

Physical Properties and Kinematics of Dense Cores Associated with Regions of Massive Star Formation from the Southern Sky

L. E. Pirogov^{a,*}, *P. M. Zemlyanukha*^a, *E. M. Dombek*^a, and *M. A. Voronkov*^b

^a Gaponov-Grekhov Institute of Applied Physics, Russian Academy of Sciences, Nizhny Novgorod, Russia

^b Commonwealth Scientific and Industrial Research Organization (CSIRO) Space and Astronomy, Epping NSW, Australia

* e-mail: pirogov@appl.sci-nnov.ru

Abstract

The results of spectral observations in the $\sim 84 - 92$ GHz frequency range of six objects in the southern sky containing dense cores and associated with regions of massive stars and star clusters formation are presented. The observations were carried out with the MOPRA-22m radio telescope. Within the framework of the local thermodynamic equilibrium (LTE) approximation, the column densities and abundances of the H^{13}CN , H^{13}CO^+ , HN^{13}C , HC_3N , $c\text{-C}_3\text{H}_2$, SiO , $\text{CH}_3\text{C}_2\text{H}$ and CH_3CN molecules are calculated. Estimates of kinetic temperatures ($\sim 30 - 50$ K), sizes of emission regions ($\sim 0.2 - 3.1$ pc) and virial masses ($\sim 70 - 4600 M_\odot$) are obtained. The linewidths in the three cores decrease with increasing distance from the center. In four cores, asymmetry in the profiles of the optically thick lines $\text{HCO}^+(1-0)$ and $\text{HCN}(1-0)$ is observed, indicating the presence of systematic motions along the line of sight. In two cases, the asymmetry can be caused by contraction of gas. The model spectral maps of $\text{HCO}^+(1-0)$ and $\text{H}^{13}\text{CO}^+(1-0)$, obtained within the framework of the non-LTE spherically symmetric model, are fitted into the observed ones. The radial profiles of density ($\propto r^{-1.6}$), turbulent velocity ($\propto r^{-0.2}$), and contraction velocity ($\propto r^{0.5}$) in the G268.42-0.85 core have been calculated. The contraction velocity profile differs from that expected both in the case of free fall of gas onto a protostar ($\propto r^{-0.5}$), and in the case of global core collapse (contraction velocity does not depend on distance). A discussion of the obtained results is provided.

Keywords: star formation, molecular clouds, dense cores, molecular lines, modeling

1 Introduction

Studies of dense cores of molecular clouds are an important tool for estimating initial conditions of the star formation process. The cores associated with the regions of formation of high-mass stars ($\gtrsim 8 M_{\odot}$) and star clusters attract special attention. Despite the greatly increased number of observations of such objects in recent years, the agreed scenario of their formation is far from complete (see, for example, [1, 2]). Compared to the regions of formation of stars with masses on the order of or less than the solar one, they are more rare, located at larger distances, evolve faster and have a hidden phase of development before the main sequence. In the early stages of evolution, massive stars actively interact with the parent dense core, increase turbulence and temperature, lead to shock waves and outflows, cause fragmentation, further compression and, under certain conditions, a new phase of star formation. Chemical composition of the gas in the regions of massive star formation is enriched due to evaporation of molecules from the surface of dust particles. The radiation of individual compact regions in water, methanol, hydroxyl and some other molecular lines may have a maser nature. The observed line profiles are significantly broadened due to turbulent and systematic motions. These effects often overlap, which complicates the interpretation of observations.

There are various assumptions about the state of the cores in which star formation occurs. Thus, in the model of a singular isothermal sphere [3, 4], it is assumed that a quasi-equilibrium spherical core with a radial Bonnor-Ebert density profile (a flat area near the center and a dependence close to r^{-2} in the shell) evolves to a state with a singularity in the center (protostar), after which a collapse begins, which spreads inside-out. In the turbulent core model [5], proposed to describe the formation of massive stars and star clusters, the initial state is considered to be a sphere in hydrostatic equilibrium, possessing supersonic turbulence and a density profile $r^{-3/2}$ [5, 6], with no systematic motions. Both in the model

of a singular isothermal sphere and in the model of a turbulent core the density and velocity radial profiles in the region where gas collapses onto a protostar in free fall are $r^{-3/2}$ and $r^{-1/2}$, respectively.

The global hierarchical collapse model [7] proceeds from the fact that cores, like parent clouds, are non-equilibrium objects that are in the process of global collapse even before the formation of a protostar, and their observed proximity to the state of virial equilibrium occurs, in particular, due to the proximity of the free fall velocity to the virial one. In this model, based on the classical works of Larson and Penston [8, 9], after the formation of a protostar, the density profile in the envelope has a form r^{-2} , and the contraction velocity is constant and does not depend on the radial distance (see, for example, [7, 10]). Since both in the quasi-equilibrium and non-equilibrium core models the density profiles in the shell are close, it is the systematic velocity profile that can serve as a factor allowing one to make a choice between the models.

Due to the inhomogeneous distribution of gas density in the cores and the presence of systematic gas motions, the observed profiles of molecular lines with large optical depth may differ from Gaussian and have an asymmetry associated with differences in the conditions affecting their excitation along the line of sight and a velocity shift due to Doppler effect. To interpret such spectra and to estimate parameters of the structure and velocity field, it is necessary to calculate excitation of molecules taking into account differences from local thermodynamic equilibrium (LTE) and compare the calculated spectra with observed ones. Among the molecular lines that are indicators of dense gas, the optically thick $\text{HCO}^+(1-0)$ and $\text{HCN}(1-0)$ lines are among the most sensitive to kinematics and density distribution.

An analysis of observational data of five massive star-forming regions in the northern sky associated with methanol masers [11] revealed an asymmetry in the profiles of the optically thick $\text{HCO}^+(1-0)$ and $\text{HCN}(1-0)$ lines in four of them. For one of the cores with signs of

contraction considered in [11] (L1287 or G121.28+0.65), we analyzed observational data in the $\text{HCO}^+(1-0)$ and $\text{HCN}(1-0)$ lines and in the lines of rarer isotopes using the non-LTE model [12]. To fit model spectral maps into observed ones, a specially developed algorithm was used, based on the methods of principal components and k-nearest neighbors [12]. Estimates of the optimal parameters of density, turbulent velocity and contraction velocity radial profiles were obtained. It turned out that the power-law index of the contraction velocity profile in L1287 is close to zero, which indicates the likelihood of a global collapse of this core. To answer the question of how typical this case is, it is necessary to conduct further studies of cores associated with regions of formation of massive stars and star clusters and showing signs of contraction.

A sample of dense cores associated with the regions of massive stars and star clusters formation in the southern sky has previously been studied in various molecular lines and in continuum [13, 14, 15, 16, 17, 18, 19, 20]. A number of physical parameters of the cores were determined, density profiles were calculated [21], estimates of the chemical composition were obtained. Also, effects of chemical differentiation were found in several objects [18].

This paper presents the results of observations of six objects from this sample in various molecular lines in the 3-mm wavelength range and the estimates of their physical characteristics and chemical composition. For two cores, where the observed $\text{HCO}^+(1-0)$ and $\text{HCN}(1-0)$ profiles have indications of gas contraction, an analysis with model calculations is given. For one of them, estimates of the parameters of the spatial distribution of density and velocity are given.

2 Sources

The objects of the study are six regions of massive star and star cluster formation in the southern sky, which we had previously observed in the $\text{CS}(2-1)$, $\text{CS}(5-4)$ [13, 18], and

$\text{N}_2\text{H}^+(1-0)$ lines [17], and in the continuum at the 1.2 mm and 350 μm wavelengths [18, 20]. The list of the sources is given in Table 1. Distances to the objects are also given there and associations with other objects are indicated.

In addition to IRAS point sources and maser sources, the cores under the study include ultracompact H II regions, near-infrared sources, submillimeter and radio sources, and molecular outflows. We calculated bolometric luminosities of the IRAS sources as an integral of the fitted curve of a “gray” body emission into the dependence of the flux on frequency [18], taking into account the distances from Table 1. Information about the presence of maser sources is taken from the *maserdb.net* database [22].

In the region G268.42–0.85, the IRAS 09002–4732 source ($L \sim 8 \times 10^4 L_\odot$) is associated with a young star cluster immersed in a dense gas and dust cloud, the dominant member of which is a star of spectral type O7 [23]. Measurements by the parallax method using the *Gaia* satellite data give a distance to the cluster of 1.7–1.8 kpc [23]. The ultracompact H II zone is associated with the cluster [26, 27]. A water maser is observed in the core [28].

The source IRAS 09018–4816 in the region G269.11–1.12 ($L \sim 6 \times 10^4 L_\odot$), associated with the ultracompact H II zone [29], is located south of the dense core. Water masers have been detected both in the direction of the core center and near the IRAS source [30, 28]. A class II methanol maser is observed near the center of the core at a frequency of 6.7 GHz [31]. Class I methanol maser lines are also observed in the core [32, 33, 34, 35, 36].

The dense core of G270.26+0.83 is associated with the RCW41 H II region which consists of two separate compact regions, the sources of which are stars of spectral types O9 V and B0 V, respectively [27]. The IRAS 09149–4743 source with a luminosity of $L \sim 5 \times 10^3 L_\odot$ is located at the periphery of the core. The core contains a cluster of young stellar objects observed as near-IR sources [37, 38], as well as water [30], class I [32, 33, 34, 35, 36] and class II methanol masers [31].

The region G285.26–0.05 consists of two cores. Core 1 contains the IRAS 10295–5746 source ($L \sim 5 \times 10^5 L_{\odot}$) and the ultracompact H II region [29], as well as a cluster of infrared 2MASS sources [39], masers of OH [40], water [41] and class II methanol [42]. Water maser is observed in core 2 [41], and there (as in core 1) an emission in the Br line was detected [43], which indicates an existence of the H II region, probably immersed in a dense dust shell.

The IRAS 11097–6102 source ($L \sim 3 \times 10^5 L_{\odot}$) is located in the central part of the extended gas and dust clump G291.27–0.71. Here is the H II region [44], the interaction of which with the parent cloud apparently determines morphology of the clump, consisting of several fragments and corresponding IR sources. Water [41] and class II methanol masers [45, 31] are observed in the region.

The region G294.97–1.73 consists of two cores. Core 1 is associated with the IRAS 11368–6312 source ($L \sim 6 \times 10^3 L_{\odot}$) and the ultracompact H II region [46]. Water masers are observed in both cores [41, 30]. In core 1, lines of class I [32, 33, 36] and class II [47] methanol masers are observed. Core 2 is associated with a class II methanol maser [31].

3 Observations

Observations of six objects from Table 1 were carried out in 2010 using the 22-m radio telescope MOPRA (Australia)¹ (project M526). During the observations, a 3-mm wavelength range receiver with an SIS mixer at the input was used. The noise temperature of the system during the observation period varied in the range $\sim 140 - 200$ K depending on the source and weather conditions. For spectral analysis, a MOPS spectrum analyzer with a total band-

¹The MOPRA telescope is part of the Australian Telescope National Foundation (ATNF). At the time of observations, it was funded by the Australian Government as a national facility managed by the Commonwealth Scientific and Industrial Research Organization (CSIRO).

width of 8 GHz² was used, which made it possible to simultaneously detect several molecular lines. The observation band was divided into 16 subbands with a width of 137.5 MHz, tuned to the lines of the HCO⁺, HCN, HNC molecules and their rarer isotopes, as well as to the lines of the HC₃N, SiO, CH₃OH, CH₃C₂H, CH₃CN and some other molecules. Each subband consisted of 4096 channels, which gave a velocity resolution of ~ 0.11 km/s. The width of the main beam of the MOPRA telescope was 36'' in this frequency range [48]. The main beam efficiency at a frequency of 86 GHz was 0.49 [48].

Mapping was carried out in the OTF mode. For each object, maps of size $2' \times 2'$ were obtained. Pointing errors were regularly checked using SiO maser observations and did not exceed $5'' \pm 2''$. The Orion KL source was used to calibrate spectral observations. Processing of the obtained data was carried out using the *Livedata* and *Gridzilla* packages³ with the help of which the 1st order baseline was subtracted, the averaging and formation of data cubes (two coordinates and velocity) with a fixed step along both coordinates (15'', Nyquist sampling) were made.

4 The results of observations

For all the observed objects, maps were obtained in the CH₃OH(5₋₁-4₀ E), c-C₃H₂(2_{1,2}-1_{0,1}), H¹³CN(1-0), H¹³CO⁺(1-0), SiO(2-1), HCN(1-0), HCO⁺(1-0), HNC(1-0) and HC₃N(10-9) lines. In the direction of the central positions of the objects, the HN¹³C(1-0), CH₃C₂H(5-4) and CH₃CN(5-4) lines were detected.

Table 2 lists the detected molecular lines in order of increasing frequency, indicating the transition, frequency, and energy of the upper level (in temperature units). Figure 1 shows the spectra in the direction of positions close to the centers of the cores, where the intensities

²The University of New South Wales digital filter bank was made available for observations on the MOPRA telescope with support from the Australian Research Council.

³<https://www.atnf.csiro.au/computing/software/livedata/index.html>

Table 1: Source List

Source	$\alpha(2000)$	$\delta(2000)$	D (kpc)	Associations with other objects
G 268.42–0.85	09 01 54.3	–47 43 59	1.7(0.1) [23]	IRAS 09002–4732
G 269.11–1.12	09 03 32.8	–48 28 39	2.6 [13]	IRAS 09018–4816
G 270.26+0.83	09 16 43.3	–47 56 36	1.3(0.2) [24]	IRAS 09149–4743, RCW 41
G 285.26–0.05	10 31 30.0	–58 02 07	4.7 [13]	IRAS 10295–5746
G 291.27–0.71	11 11 49.9	–61 18 14	2.8(0.3) [25]	IRAS 11097–6102, NGC 3576, RCW 57
G 294.97–1.73	11 39 12.6	–63 28 47	1.2 [13]	IRAS 11368–6312

The distances to G268.42, G291.27 were obtained by the parallax method using data from the *Gaia* satellite, the distance to G270.26 was estimated by the spectroscopic method, and kinematic distances are given for the remaining objects. Since the error values of the latter are not given in the literature, in the calculations we arbitrarily took them equal to 0.3 kpc (G269.11 and G294.97) and 0.5 kpc (G285.26). Here and below, abbreviated names of objects are used. The numbers in parentheses following the names G285.26 and G294.97 correspond to individual cores.

of most lines are close to maximum. For the regions G285.26 and G297.97, which contain two compact cores, the spectra are shown in the direction of the central positions of each of them. The vertical dashed line in each diagram corresponds to the center of the optically thin $\text{H}^{13}\text{CO}^+(1-0)$ line. It can be seen that the profiles of the optically thick lines $\text{HCO}^+(1-0)$, $\text{HCN}(1-0)$ and $\text{HNC}(1-0)$ in G268.42, G269.11, G270.26 and G291.27 are asymmetric. In G268.42 and G269.11 there is a pronounced absorption dip between the blue and red peaks, and the intensity of the blue peak exceeds the intensity of the red one.

4.1 Maps in molecular lines

Integrated intensity maps of various molecular lines are shown in Figs. 2,3,4,5,6,7. The figures show the IRAS sources and the masers of water, class II methanol and hydroxyl which exist in the cores and are indicators of the regions of massive star formation. The figures also show maps of dust emission in the continuum at a wavelength of $350 \mu\text{m}$ [20], obtained with significantly better angular resolution and allowing the internal structure of cores to be estimated in more detail.

Table 2: List of observed molecular lines

Molecule	Transition	Frequency (MHz)	E_u/k (K)
CH ₃ OH	5 ₋₁ -4 ₀ E	84521.206	40.39
c-C ₃ H ₂	2 _{1,2} -1 _{0,1}	85338.906	6.45
CH ₃ C ₂ H	5 ₃ -4 ₃	85442.600	77.34
CH ₃ C ₂ H	5 ₂ -4 ₂	85450.765	41.21
CH ₃ C ₂ H	5 ₁ -4 ₁	85455.665	19.53
CH ₃ C ₂ H	5 ₀ -4 ₀	85457.299	12.30
H ¹³ CN	1-0 $F=1-1$	86338.737	4.14
H ¹³ CN	1-0 $F=2-1$	86340.176	4.14
H ¹³ CN	1-0 $F=0-1$	86342.255	4.14
H ¹³ CO ⁺	1-0	86754.288	4.16
SiO	2-1	86846.995	6.25
HN ¹³ C	1-0 $F=2-1$	87090.859	4.18
HCN	1-0 $F=1-1$	88630.416	4.25
HCN	1-0 $F=2-1$	88631.847	4.25
HCN	1-0 $F=0-1$	88633.936	4.25
HCO ⁺	1-0	89188.526	4.28
HNC	1-0	90663.564	4.35
HC ₃ N	10-9	90978.989	24.01
CH ₃ CN	5 ₃ -4 ₃	91971.130	77.55
CH ₃ CN	5 ₂ -4 ₂	91979.994	41.83
CH ₃ CN	5 ₁ -4 ₁	91985.314	20.39
CH ₃ CN	5 ₀ -4 ₀	91987.088	13.24

In most cases, the emission regions in different lines are spatially correlated with each other. The best correlation is observed between the HCO⁺(1-0), HCN(1-0), HNC(1-0), and HC₃N(10-9) maps as well as between the maps of the isotopes H¹³CO⁺(1-0), H¹³CN(1-0). The maps in the c-C₃H₂(2_{1,2}-1_{0,1}) and SiO(2-1) lines are less correlated with the others. Continuum maps at 350 μ m are in most cases within half-intensity molecular emission contours. The IRAS sources are located both near the centers of the cores and at the periphery (in G269.11 and G270.26). Maser sources are observed in all cores, indicating star formation.

To estimate the sizes of emission regions, the convolution of a two-dimensional Gaussian

elliptical function with unknown parameters and a two-dimensional circular Gaussian with a width equal to the width of the main beam of the telescope radiation pattern is fitted into integrated intensity maps [17]. The sizes of the cores are determined as the geometric mean of the sizes of the fitted elliptic two-dimensional Gaussian. The centers of the emission regions are generally close to each other within the size of the telescope main beam. Their morphology generally correlates with the morphology of the 350 μm continuum maps (with the exception of G291.27), although it should be noted that the latter are significantly smaller in size. The ratios of the axes of the fitted ellipses, the angular sizes of the emission regions in various lines at half the maximum intensity level are given below in Table 6 along with the errors in their determination.

4.2 Line parameters

We processed spectral data using standard methods with a help of the GILDAS package ⁴ and our original programs. After subtracting baseline from the spectral subranges with lines, Gaussian functions (one or more) are fitted (approximated) into the observed spectra to determine intensity, velocity along the line of sight corresponding to the center of the line, and line width at half the maximum intensity (FWHM). The parameters of the observed molecular lines in the direction of the positions of the emission peaks are given in Table 3. When processing the CH₃C₂H(5–4) and CH₃CN(5–4) spectra, the distances between lines with different quantum numbers K are fixed, and their widths are considered identical. The same procedure is used to process the spectra of H¹³CN(1–0), consisting of three close hyperfine components. For the lines with large optical depth (HCN(1–0), HCO⁺(1–0), HNC(1–0)), the profiles of which are in many cases non-Gaussian, Table 3 shows only integrated intensities. The uncertainties of integrated intensities are calculated as $\Delta T_{MB} \sqrt{N_{ch}} \delta V_{ch}$, where ΔT_{MB} is the noise level in the channel without a line (calculated after subtracting the baseline), N_{ch} is the number of channels with the line, and δV_{ch} is the velocity resolution (channel width).

⁴<http://iram.fr/IRAMFR/GILDAS>

5 Physical parameters of cores

5.1 Kinetic temperatures

The methyl acetylene ($\text{CH}_3\text{C}_2\text{H}$) and methyl cyanide (CH_3CN) lines can be used to determine kinetic temperatures in dense cores. For molecules of the symmetric top type, such as these molecules, transitions with different quantum numbers consist of several lines with different values of the quantum number K , which determines the projection of the angular momentum on the axis of symmetry of the molecule. Approximating the dependence of the integrated intensities of lines with different K on energy levels with a straight line, the rotational temperature can be determined by the slope coefficient and used as an estimate of the kinetic temperature (see, for example, [49]). Kinetic temperatures are calculated by this method for five cores (see Table 4), in which at least two $\text{CH}_3\text{C}_2\text{H}(5-4)$ lines with different K values are reliably detected. Three cores are selected for estimates using the $\text{CH}_3\text{CN}(5-4)$ lines (see Table 4). All these lines appear to be optically thin. This is confirmed by the fact that their intensities lie in the intensity ranges of the corresponding lines observed in regions of formation of massive stars, the optical depth of which is small (see, for example, [50, 51]). The product of the T_{MB} and ΔV values, which are determined from the approximation, is taken as the integrated intensities of lines with different K . The kinetic temperature errors are calculated by the method of error propagation from approximation errors. Due to the relatively low signal-to-noise ratios in the observations of $\text{CH}_3\text{C}_2\text{H}(5-4)$ and $\text{CH}_3\text{CN}(5-4)$ ($\lesssim 3$), the temperature errors turned out to be quite high (of the order of the values themselves). To reduce them, temperatures in four of the five cores are calculated from spectra averaged over several nearby points (averaging ranges are indicated in the 2nd and 3rd columns of Table 4).

Table 4 shows the calculated kinetic temperatures. The obtained values are $\sim 30 - 40$ K,

Table 3: Parameters of the observed lines

Линия	I (K km s ⁻¹)	T_{MB} (K)	V_{LSR} (km s ⁻¹)	ΔV (km s ⁻¹)	I (K km s ⁻¹)	T_{MB} (K)	V_{LSR} (km s ⁻¹)	ΔV (km s ⁻¹)
	G 268.42–0.85 (0'',–15'')				G 269.11–1.12 (15'',30'')			
CH ₃ OH(5 ₋₁ –4 ₀ E)	1.67(0.12)	0.51(0.04)	2.95(0.12)	3.21(0.30)	4.47(0.15)	1.38(0.05)	10.25(0.05)	2.86(0.12)
c-C ₃ H ₂ (2 _{1,2} –1 _{0,1})	1.28(0.14)	0.37(0.04)	2.60(0.17)	3.24(0.42)	1.72(0.15)	0.44(0.04)	10.37(0.17)	3.88(0.42)
CH ₃ C ₂ H(5 ₀ –4 ₀)	1.46(0.16)	0.46(0.05)	3.00(0.09)	1.94(0.22)	1.44(0.19)	0.23(0.03)	10.10(0.18)	2.98(0.40)
H ¹³ CN(1–0 $F=2-1$)	3.36(0.21)	0.61(0.04)	2.98(0.08)	2.81(0.18)	4.12(0.20)	0.75(0.04)	10.40(0.08)	3.06(0.17)
H ¹³ CO ⁺ (1–0)	2.53(0.11)	0.96(0.05)	2.99(0.06)	2.73(0.16)	2.65(0.11)	0.75(0.04)	10.29(0.08)	3.40(0.20)
SiO(2–1)	1.00(0.13)	0.21(0.03)	3.02(0.34)	4.56(0.90)	0.77(0.12)	0.31(0.04)	10.54(0.18)	2.67(0.45)
HN ¹³ C(1–0)	0.91(0.11)	0.34(0.05)	3.22(0.16)	2.40(0.38)	1.10(0.14)	0.39(0.05)	10.32(0.15)	2.68(0.38)
HCN(1–0 $F=2-1$)	38.6(0.2)				34.6(0.3)			
HCO ⁺ (1–0)	20.5(0.2)				26.9(0.2)			
HNC ⁺ (1–0)	15.0(0.1)				16.5(0.2)			
HC ₃ N(10–9)	3.53(0.10)	1.40(0.04)	2.82(0.03)	2.43(0.08)	5.21(0.12)	1.68(0.04)	10.21(0.03)	2.90(0.08)
CH ₃ CN(5 ₀ –4 ₀)	0.75(0.09)	0.11(0.02)	3.05(0.30)	4.11(0.58)	1.04(0.13)	0.16(0.02)	10.55(0.23)	3.83(0.46)
	G 270.26+0.83 (–15'',30'')				G 291.27–0.71 (–30'',–45'')			
CH ₃ OH(5 ₋₁ –4 ₀ E)	6.78(0.10)	2.22(0.04)	10.04(0.02)	2.74(0.06)	2.77(0.13)	0.91(0.04)	–23.58(0.06)	2.72(0.15)
c-C ₃ H ₂ (2 _{1,2} –1 _{0,1})	1.02(0.10)	0.31(0.04)	10.01(0.17)	3.13(0.43)	2.57(0.18)	0.48(0.03)	–23.06(0.16)	5.00(0.39)
CH ₃ C ₂ H(5 ₀ –4 ₀)	0.84(0.13)	0.14(0.03)	9.20(0.26)	3.36(0.54)	3.35(0.21)	0.42(0.04)	–23.96(0.09)	2.80(0.22)
H ¹³ CN(1–0 $F=2-1$)	3.12(0.16)	0.50(0.03)	9.66(0.10)	3.29(0.19)	4.08(0.22)	0.61(0.03)	–23.95(0.09)	3.31(0.16)
H ¹³ CO ⁺ (1–0)	2.06(0.10)	0.67(0.04)	9.62(0.07)	2.85(0.18)	3.66(0.11)	1.11(0.04)	–23.72(0.05)	3.09(0.12)
SiO(2–1)	1.33(0.10)	0.38(0.03)	10.28(0.16)	4.24(0.42)	2.42(0.14)	0.50(0.03)	–23.42(0.13)	4.42(0.32)
HN ¹³ C(1–0)	0.75(0.10)	0.21(0.03)	9.64(0.28)	3.81(0.73)	1.41(0.13)	0.46(0.04)	–23.57(0.11)	2.82(0.28)
HCN(1–0 $F=2-1$)	28.9(0.2)	7.5(0.1)	10.02(0.01)	2.15(0.03)	54.4(0.3)	5.50(0.07)	–23.37(0.03)	4.33(0.05)
HCO ⁺ (1–0)	25.9(0.2)	10.6(0.1)	9.92(0.01)	2.44(0.03)	45.2(0.2)	8.20(0.05)	–23.10(0.01)	5.04(0.03)
HNC ⁺ (1–0)	13.0(0.1)	4.6(0.1)	9.86(0.01)	2.55(0.03)	22.4(0.1)	5.00(0.03)	–23.46(0.01)	4.09(0.03)
HC ₃ N(10–9)	2.58(0.10)	0.75(0.03)	9.70(0.07)	3.46(0.18)	5.73(0.12)	2.01(0.04)	–23.97(0.03)	2.59(0.06)
CH ₃ CN(5 ₀ –4 ₀)	1.16(0.12)	0.16(0.02)	9.54(0.17)	3.30(0.35)	1.62(0.14)	0.23(0.03)	–24.03(0.12)	3.00(0.27)

Table 3: Parameters of the observed lines (continued)

Линия	I (K km s ⁻¹)	T_{MB} (K)	V_{LSR} (km s ⁻¹)	ΔV (km s ⁻¹)	I (K km s ⁻¹)	T_{MB} (K)	V_{LSR} (km s ⁻¹)	ΔV (km s ⁻¹)
	G 285.26–0.05 (0'',–15'')				G 285.26–0.05 (–45'',–75'')			
CH ₃ OH(5 ₋₁ –4 ₀ E)	<0.4				1.92(0.18)	0.50(0.05)	1.37(0.21)	4.53(0.55)
c-C ₃ H ₂ (2 _{1,2} –1 _{0,1})	1.28(0.15)	0.22(0.03)	2.28(0.45)	7.19(1.34)	1.62(0.19)	0.44(0.05)	2.84(0.21)	3.64(0.53)
CH ₃ C ₂ H(5 ₀ –4 ₀)	< 0.9				< 1.1			
H ¹³ CN(1–0 $F=2-1$)	0.92(0.22)	0.12(0.04)	2.68(1.11)	5.26(2.05)	1.19(0.31)	0.34(0.06)	2.64(0.19)	2.26(0.46)
H ¹³ CO ⁺ (1–0)	0.57(0.13)	0.25 (0.05)	3.45(0.24)	2.31(0.58)	1.33(0.14)	0.45(0.05)	2.53(0.16)	2.84(0.40)
SiO(2–1)	0.97(0.13)	0.1 (0.03)	4.23(0.48)	6.47(1.38)	<0.5			
HN ¹³ C(1–0)	< 0.4				< 0.5			
HCN(1–0)	32.9(0.2)	3.82(0.04)	2.93(0.03)	4.37(0.05)	31.0(0.3)	4.01(0.05)	2.55(0.03)	3.92(0.05)
HCO ⁺ (1–0)	27.0(0.2)	5.17(0.05)	3.05(0.02)	4.78(0.05)	25.2(0.2)	5.55(0.05)	2.55(0.02)	4.29(0.05)
HNC ⁺ (1–0)	6.8(0.2)	1.52(0.03)	3.14(0.05)	4.28(0.12)	10.5(0.2)	2.78(0.05)	2.51(0.03)	3.47(0.07)
HC ₃ N(10–9)	0.65(0.11)	0.19(0.03)	3.21(0.34)	4.48(0.88)	1.63(0.14)	0.64(0.05)	2.07(0.10)	2.56(0.26)
CH ₃ CN(5 ₀ –4 ₀)	< 0.9				< 0.9			
	G 294.97–1.73 (15'',–15'')				G 294.97–1.73 (60'',15'')			
CH ₃ OH(5 ₋₁ –4 ₀ E)	1.42(0.12)	0.63(0.05)	–8.08(0.08)	2.10(0.20)	0.51(0.12)	0.25(0.05)	–8.47(0.18)	1.79(0.44)
c-C ₃ H ₂ (2 _{1,2} –1 _{0,1})	1.61(0.14)	0.51(0.04)	–8.83(0.12)	2.82(0.29)	1.07(0.14)	0.37(0.04)	–9.35(0.16)	2.92(0.41)
CH ₃ C ₂ H(5 ₀ –4 ₀)	1.09(0.14)	0.26(0.04)	–8.14(0.11)	1.89(0.26)	< 0.6			
H ¹³ CN(1–0 $F=2-1$)	1.23(0.19)	0.41(0.05)	–8.31(0.09)	1.73(0.23)	1.19(0.19)	0.28(0.04)	–8.89(0.17)	2.41(0.44)
H ¹³ CO ⁺ (1–0)	1.25(0.11)	0.64(0.05)	–8.39(0.07)	1.82(0.17)	1.29(0.10)	0.51(0.05)	–9.00(0.11)	2.49(0.27)
SiO(2–1)	0.47(0.11)	0.14(0.04)	–8.17(0.38)	3.23(0.98)	<0.4			
HN ¹³ C(1–0)	0.72(0.13)	0.46(0.06)	–8.26(0.10)	1.57(0.25)	0.48(0.12)	0.35(0.06)	–8.53(0.12)	1.44(0.30)
HCN(1–0)	31.5(0.2)	5.45(0.05)	–8.49(0.01)	3.22(0.03)	25.5(0.2)	4.36(0.04)	–9.22(0.01)	3.18(0.03)
HCO ⁺ (1–0)	24.9(0.2)	6.73(0.05)	–8.48(0.01)	3.38(0.03)	20.9(0.2)	6.14(0.05)	–9.16(0.01)	3.15(0.03)
HNC ⁺ (1–0)	12.2(0.1)	3.91(0.04)	–8.43(0.01)	2.90(0.03)	9.4(0.1)	3.02(0.04)	–9.18(0.02)	2.83(0.05)
HC ₃ N(10–9)	2.76(0.10)	1.32(0.05)	–8.30(0.03)	1.89(0.08)	1.81(0.11)	0.89(0.05)	–8.90(0.05)	1.89(0.12)
CH ₃ CN(5 ₀ –4 ₀)	< 0.5				< 0.5			

The CH₃C₂H(5₀–4₀) parameters are calculated for the spectra averaged over the following regions: $\Delta\alpha$: [0'' ÷ 30''], $\Delta\delta$: [15'' ÷ 45''] (G269.11); $\Delta\alpha$: [–15'' ÷ 0''], $\Delta\delta$: [0'' ÷ 30''] (G270.26); $\Delta\alpha$: [–15'' ÷ 15''], $\Delta\delta$: [–30'' ÷ 0''] (G294.97).

The CH₃CN(5₀–4₀) parameters are calculated for the spectra averaged over the following regions: $\Delta\alpha$: [–30'' ÷ 30''] and $\Delta\delta$: [–30'' ÷ 30''] (G268.42); $\Delta\alpha$: [0'' ÷ 30''], $\Delta\delta$: [15'' ÷ 45''] (G269.11); $\Delta\alpha$: [–15'' ÷ –30''] and $\Delta\delta$: [–30'' ÷ 45''] (G291.27).

The integrated intensities of CH₃C₂H(5–4), H¹³CN(1–0), HCN(1–0) and CH₃CN(5–4) are calculated using all components of the spectra.

the estimates from $\text{CH}_3\text{C}_2\text{H}(5-4)$ and $\text{CH}_3\text{CN}(5-4)$ coincide within the error for G269.11 and G270.26. For G291.27, the temperature estimate from $\text{CH}_3\text{C}_2\text{H}(5-4)$ reaches ~ 50 K, while the estimate from $\text{CH}_3\text{CN}(5-4)$ is ~ 35 K. This discrepancy is discussed in Section 7. Thermal linewidths corresponding to the temperature estimates for H^{13}CO^+ are $\sim 0.2 - 0.3$ km/s for $T_{\text{KIN}} = 30 - 50$ K.

Table 4: Kinetic temperatures

Source	$\Delta\alpha('')$	$\Delta\delta('')$	T_{KIN} (K) ($\text{CH}_3\text{C}_2\text{H}$)	T_{KIN} (K) (CH_3CN)
G 268.42–0.85	0	–15	32(8)	
G 269.11–1.12	0 \div 30	15 \div 45	33(12)	44(13)
G 270.26+0.83	–15 \div 0	15 \div 30	27(15)	56(34)
G 291.27–0.71	–30 \div –15	–45 \div –30	51(8)	36(7)
G 294.97–1.73	–15 \div 15	–30 \div 0	48(17)	

Kinetic temperatures for all the objects except G268.42–0.85 are calculated from spectra averaged in the indicated $\Delta\alpha$ and $\Delta\delta$ ranges.

5.2 Column densities and molecular abundances

Using integrated intensities of optically thin lines, it is possible to estimate the number of molecules along the line of sight in the local thermodynamic equilibrium (LTE) approximation [52, 11]. We calculated the H^{13}CN , H^{13}CO^+ , HN^{13}C , HC_3N , *c*- C_3H_2 , SiO, $\text{CH}_3\text{C}_2\text{H}$, and CH_3CN column densities towards the positions of maximum intensity in the objects. The excitation temperature is taken to be 10 K for all lines except $\text{CH}_3\text{C}_2\text{H}(5-4)$ and $\text{CH}_3\text{CN}(5-4)$. With this value, the calculated values of N_{MOL} are close to the minimum. If the excitation temperature is different from 10 K, column densities can be up to several times higher. For $\text{CH}_3\text{C}_2\text{H}(5-4)$ and $\text{CH}_3\text{CN}(5-4)$, estimates of kinetic temperatures are taken as excitation

temperatures (see Section 5.1). The calculated values of molecular column densities are given in Table 5. Their analysis indicates that $N(\text{H}^{13}\text{CN})$, $N(\text{H}^{13}\text{CO}^+)$ and $N(\text{HC}_3\text{N})$ in G285.26 and G294.97 are several times lower compared to the rest. The column densities of $\text{c-C}_3\text{H}_2$ and SiO do not vary much from object to object.

To estimate molecular abundances ($X = N_{\text{MOL}}/N(\text{H}_2)$), we used the values of molecular hydrogen column densities, calculated from the 1.2 mm continuum observations [18] which were obtained with an angular resolution of $24''$. Dust temperatures are taken equal to 30 K for all the objects except G285.26(2) (20 K) and G268.42 (35 K), which is consistent with the estimates made in [18, 20] for the value of β , the power-law index of the dependence of the dust emissivity on frequency, equal to 2. The resulting column densities of molecular hydrogen are given in Table 5. Their errors are associated mainly with uncertainty in β , which affects the estimates of dust temperatures and for most objects can be $\sim 20\%$ for the temperature variations of ± 5 K (an effect of β on dust temperature estimates is discussed, for example, in [20]). For G285.26(2) at the dust temperature of 15 K, the calculated column density of hydrogen is higher by 50% compared to the column density calculated for 20 K. The molecular abundance values are given in Table 5. They lie in the following ranges: $X(\text{C}_3\text{H}_2) \simeq (0.2-1.2) 10^{-10}$, $X(\text{CH}_3\text{C}_2\text{H}) \simeq (0.6-1.5) 10^{-9}$, $X(\text{CH}_3\text{CN}) \simeq (1.2-4.6) 10^{-11}$, $X(\text{H}^{13}\text{CN}) \simeq (0.8-9.2) 10^{-11}$, $X(\text{H}^{13}\text{CO}^+) \simeq (0.3-3.5) 10^{-11}$, $X(\text{H}_3\text{CN}) \simeq (2.3-45.9) 10^{-11}$, $X(\text{HN}^{13}\text{C}) \simeq (0.6-2.3) 10^{-11}$, $X(\text{SiO}) \simeq (0.7-3.3) 10^{-11}$. The lowest abundances of H^{13}CN , H^{13}CO^+ and H_3CN are observed in the G285.26(1) core.

5.3 Sizes, velocity dispersions and virial masses of the cores

Table 6 shows the axes ratio of the fitted ellipses, the angular and linear dimensions of the emission regions at half the maximum intensity level, obtained from the approximation of the maps. The emission regions in the G270.26 core are, on average, closest to a spherically

Table 5: Column densities and molecular abundances

Molecule	N, cm^{-2}	X	N, cm^{-2}	X	N, cm^{-2}	X	N, cm^{-2}	X
	($\times 10^{12}$)	($\times 10^{-11}$)	($\times 10^{12}$)	($\times 10^{-11}$)	($\times 10^{12}$)	($\times 10^{-11}$)	($\times 10^{12}$)	($\times 10^{-11}$)
	G268.42(0'', -15'')		G269.11(15'', 30'')		G270.26(-15'', 30'')		G291.27(-30'', -45'')	
H ¹³ CN	6.6	2.2	8.1	9.2	6.1	5.6	8.0	5.0
H ¹³ CO ⁺	2.9	1.0	3.1	3.5	2.4	2.2	4.2	2.6
SiO	2.3	0.7	1.7	1.9	2.9	2.6	5.3	3.3
HN ¹³ C	1.7	0.6	2.1	2.3	1.4	1.3	2.6	1.7
HC ₃ N	27.4	9.1	40.0	45.9	20.0	18.2	44.5	27.8
CH ₃ C ₂ H	460	153	94.2	107	64.6	58.7	162	101
CH ₃ CN	3.5	1.2	4.0	4.6	3.5	3.2	4.5	2.8
c-C ₃ H ₂	6.3	2.1	8.5	9.6	5.0	4.6	12.6	7.9
H ₂ ¹	30		8.8		11		16	
	G285.26(0'', -15'')		G285.26(-45'', -75'')		G294.97(15'', -15'')		G294.97(60'', 15'')	
H ¹³ CN	1.8	0.8	2.3	2.9	2.4	3.6	2.3	3.6
H ¹³ CO ⁺	0.6	0.3	1.5	1.9	1.4	2.1	1.5	2.3
SiO	2.1	1.0			1.0	1.5		
HN ¹³ C					1.4	2.0	0.9	1.4
HC ₃ N	5.0	2.3	12.6	15.8	21.4	31.5	6.9	10.6
CH ₃ C ₂ H					67.5	99.3		
c-C ₃ H ₂	6.3	2.9	8.0	1.0	7.9	11.6	5.3	8.1
H ₂ ¹	22		8.0		6.8		6.5	

¹ The H₂ column density values should be multiplied by 10²².

symmetrical shape; the emission regions in G294.97(2) are the most elongated. On average, the HC₃N(10–9) and CH₃OH(5₋₁–4₀ E) emission regions are the most compact. Thus, in G270.26, G285.26(2), G294.97(1) their sizes are $\sim 1.5 - 2$ times smaller than the emission regions in other lines (see Table 6). In G268.42, a compact emission region of SiO(2–1) with a size of 0.2 pc is observed.

Table 6 shows the line widths averaged over areas within the half-maximum intensity contour. The line widths (in most cases $\sim 2 - 3$ km/s) are significantly higher than thermal ones. The SiO(2–1) lines, which are indicators of shock waves in the shells surrounding

young stars (e.g., [15]), are the most broad ($\sim 3 - 5$ km/s).

The virial masses given in the last column of Table 6, are determined from the values of the emission region sizes and velocity dispersions (averaged line widths), as $M_{\text{VIR}}(M_{\odot}) = 105 \langle \Delta V \rangle^2 d$, where ΔV and d are taken in km/s and in pc, respectively (see, for example, [17]). This expression is valid for spherically symmetric cores with constant density in the absence of external pressure and magnetic field. Virial masses of the cores, calculated from the lines of rare isotopes, the optical depth of which is apparently less than unity ($\text{H}^{13}\text{CN}(1-0)$, $\text{H}^{13}\text{CO}^+(1-0)$, $\text{HN}^{13}\text{C}(1-0)$), vary from hundreds of solar masses (G270.26, G294.97) to $\gtrsim 1000 M_{\odot}$ (G285.26, G291.27).

Table 6: Physical parameters of the cores

Line	Axes ratio	$\Delta\Theta$ (")	d (pc)	$\langle\Delta V\rangle$ (km s ⁻¹)	M_{VIR} (M_{\odot})
G268.42-0.85					
CH ₃ OH	1.9(0.2)	61.3(3.8)	0.51(0.04)	2.8(0.1)	420(46)
c-C ₃ H ₂	1.4(0.2)	103.9(8.2)	0.86(0.08)	3.1(0.2)	860(140)
H ¹³ CN	1.2(0.1)	73.8(3.6)	0.61(0.05)	2.6(0.1)	430(47)
H ¹³ CO ⁺	2.0(0.1)	67.5(1.8)	0.56(0.04)	2.0(0.1)	234(28)
SiO	2.1(1.5)	27(10)	0.22(0.08)	4.9(0.2)	560(215)
HN ¹³ C	2.7(0.4)	98.4(6.9)	0.81(0.07)	2.1(0.2)	380(80)
HCN	1.12(0.04)	74.0(1.3)	0.61(0.04)		
HCO ⁺	1.04(0.03)	66.2(1.1)	0.55(0.03)		
HNC	1.4(0.1)	69.7(1.6)	0.57(0.04)		
HC ₃ N	1.4(0.1)	67.1(1.9)	0.55(0.04)	2.0(0.1)	230(28)
G269.11-1.12					
CH ₃ OH	2.2(0.3)	41.5(2.7)	0.52(0.07)	2.5(0.1)	340(53)
H ¹³ CN	2.1(0.3)	51.2(3.5)	0.65(0.09)	2.7(0.1)	490(76)
H ¹³ CO ⁺	2.8(0.7)	38.7(4.7)	0.49(0.08)	2.4(0.1)	300(55)
SiO	1.8(0.5)	38.0(4.9)	0.48(0.08)	3.2(0.5)	515(180)
HN ¹³ C	3.8(1.6)	32.9(7.1)	0.41(0.10)	2.4(0.1)	250(65)
HCN	1.7(0.2)	73.3(3.3)	0.92(0.11)		
HCO ⁺	2.4(0.2)	66.1(1.8)	0.83(0.10)		
HNC	2.0(0.1)	60.1(1.9)	0.76(0.09)		
HC ₃ N	2.5(0.2)	60.0(2.4)	0.76(0.09)	2.7(0.1)	580(83)

5.4 Radial velocity dispersion profiles

Line widths obtained from Gaussian fitting the spectra significantly exceed thermal widths (see Table 6), so they can be approximately used as an estimate of the dispersions of non-thermal velocities in sources. This parameter is used in theoretical models that include non-thermal motions of gas in the cores (e.g., [5, 7]), in the equation of state of gas in turbulent cores (e.g., [53, 21]) as well as for calculating virial masses and virial parameters used to estimate the stability of cores and clouds (e.g., [54, 55]).

To estimate spatial variations of velocity dispersions, the dependences of averaged line widths on impact parameters are calculated. When averaging, the width values higher than 3σ are used, where σ is the error obtained from the Gaussian fitting (see Table 3). The impact parameter (b) is calculated as a square root of A/π , where A is the area of the region that includes all points with intensity above a given level, the value of which varied from I_{MAX} to $0.05 I_{MAX}$ with increments of $0.01 I_{MAX}$. If the difference $b_i - b_{i-1}$ becomes greater than half the mapping step ($7.5''$), then the average line width and its error are calculated for this area (the calculation method is described in more detail in [56, 17]).

Figure 8 shows the dependences of the average widths of the optically thin $\text{H}^{13}\text{CO}^+(1-0)$, $\text{H}^{13}\text{CN}(1-0)$ lines, as well as the $\text{HC}_3\text{N}(10-9)$ lines. The emission regions in these lines are spatially correlated with each other and are relatively extended. The number of averaged line width values increases with increasing b from 1 in the center to $\sim 10 - 15$ at the edge (for the cores in the G285.26 and G294.97 regions, the number of averaged values at the edge is $\sim 5 - 10$). In three cases (G268.42, G269.11 and G270.26), the line widths decrease with increasing impact parameter from the direction to the center to $b \sim 0.3 - 0.6$ pc. The difference between the line widths in the center and at the edges in these cores reaches $\sim 1.5 - 2$ km/s. No similar trends are found in G285.26(1, 2), G291.27, and G294.97(1, 2).

The broadening of lines in the center of the cores may be partly due to an increase in

Table 6: Physical parameters of the cores (continued)

Line	Axes ratio	$\Delta\Theta$ ($''$)	d (pc)	$\langle\Delta V\rangle$ (km s^{-1})	M_{VIR} (M_{\odot})
G270.26+0.83					
CH ₃ OH	1.3(0.2)	27.6(1.9)	0.17(0.03)	2.7(0.1)	133(25)
c-C ₃ H ₂	1.3(0.3)	121(13)	0.76(0.14)	2.0(0.1)	320(68)
H ¹³ CN	1.2(0.2)	40.6(3.4)	0.26(0.04)	2.8(0.2)	210(48)
H ¹³ CO ⁺	1.1(0.1)	46.3(2.6)	0.29(0.05)	2.0(0.1)	123(24)
SiO	1.6(0.5)	43.0(6.1)	0.27(0.06)	3.4(0.4)	330(100)
HN ¹³ C	1.8(0.2)	69.3(4.6)	0.44(0.07)	3.2(0.2)	470(100)
HCN	1.4(0.1)	64.7(1.5)	0.41(0.06)		
HCO ⁺	1.4(0.1)	59.6(1.3)	0.38(0.06)		
HNC	1.2(0.1)	60.3(1.4)	0.38 0.06		
HC ₃ N	1.1(0.2)	31.5(2.8)	0.20(0.04)	2.5(0.2)	130(30)
G291.27-0.71					
CH ₃ OH	1.3(0.3)	74(9)	1.0(0.2)	3.0(0.1)	950(170)
c-C ₃ H ₂	1.8(0.1)	103(18)	1.4(0.3)	5.6(0.2)	4600(1000)
H ¹³ CN	1.9(0.4)	46.0(4.3)	0.6(0.1)	3.3(0.1)	710(110)
H ¹³ CO ⁺	1.7(0.1)	76.2(2.5)	1.0(0.1)	3.0(0.1)	980(130)
SiO	1.9(0.2)	74.9(4.3)	1.0(0.1)	4.9(0.1)	2600(330)
HN ¹³ C	1.8(0.2)	78.4(5.0)	1.1(0.1)	2.8(0.1)	880(130)
HCN	1.7(0.2)	120(6)	1.6(0.2)		
HCO ⁺	1.7(0.1)	128(5)	1.7(0.2)		
HNC	1.9(0.2)	97.7(4.1)	1.3(0.2)		
HC ₃ N	1.4(0.2)	70.2(3.8)	1.0(0.1)	2.5(0.1)	630(90)

Table 6: Physical parameters of the cores (continued)

Line	Axes ratio	$\Delta\Theta$ (")	d (pc)	$\langle\Delta V\rangle$ (km s ⁻¹)	M_{VIR} (M_{\odot})
G285.26–0.05 (1)					
H ¹³ CN	2.0(0.6)	84(13)	1.9(0.4)	3.6(0.4)	2600(760)
SiO	1.6(0.4)	41.7(5.6)	1.0(0.2)	4.7(1.0)	2200(1000)
HCN	2.1(0.3)	50.6(4.2)	1.2(0.2)		
HCO ⁺	2.3(0.5)	36.6(4.2)	0.8(0.1)		
G285.26–0.05 (2)					
CH ₃ OH	2.0(0.3)	54.3(3.9)	1.2(0.2)	3.4(0.3)	1500(330)
<i>c</i> -C ₃ H ₂	1.0(0.4)	68(12)	1.5(0.3)	4.0(0.1)	2600(550)
HCN	1.9(0.7)	135(24)	3.1(0.6)		
HCO ⁺	1.6(0.3)	107(9)	2.4(0.3)		
HNC	1.5(0.8)	120(30)	2.7(0.7)		
HC ₃ N	4.2(1.4)	36.4(6.2)	0.8(0.2)	2.4(0.1)	500(110)
G294.97–1.73 (1)					
CH ₃ OH	1.8(0.3)	34.5(3.3)	0.20(0.05)	2.1(0.1)	90(30)
<i>c</i> -C ₃ H ₂	2.1(0.3)	75.1(5.4)	0.4(0.1)	2.5(0.1)	290(80)
H ¹³ CN	2.0(0.7)	86(16)	0.5(0.2)	1.9(0.1)	190(60)
H ¹³ CO ⁺	1.1(0.5)	44(10)	0.3(0.1)	2.0(0.1)	110(40)
SiO	1.4(1.3)	84(10)	0.5(0.1)	3.2(0.1)	530(150)
HN ¹³ C	1.6(0.3)	59.3(5.4)	0.3(0.1)	1.4(0.1)	70(20)
HCN	1.5(0.1)	90.9(3.2)			
HCO ⁺	1.5(0.1)	78.2(3.2)			
HNC	1.5(0.1)	65.7(2.7)			
HC ₃ N	1.6(0.2)	49.1(2.5)	0.3(0.1)	1.88(0.04)	110(30)
G294.97–1.73 (2)					
H ¹³ CO ⁺	4.0(1.1)	70(10)	0.4(0.1)	2.6(0.1)	290(90)
HCO ⁺	3.2(1.2)	124(24)			
HNC	3.4(1.2)	95(16)			
HC ₃ N	2.7(0.7)	80(10)	0.5(0.1)	1.93(0.04)	180(50)

the optical depth. Indeed, optical depth ~ 1 can lead to broadening of Gaussian profiles by a factor of ~ 1.2 due to saturation (e.g., [57]). However, it is hardly possible to completely explain the found trends in G268.42, G269.11 and G270.26 by optical depth effects. Note, that the widths of the $\text{H}^{13}\text{CN}(1-0)$ lines exceed the widths of other lines in G268.42, G270.26, G291.27 and G294.97(1), while the widths of the $\text{HC}_3\text{N}(10-9)$ lines are close to the corresponding widths of $\text{H}^{13}\text{CO}^+(1-0)$, or less than them (G291.27, G294.97(2)).

A possible explanation for the obtained trends is an increase in the degree of dynamic activity (turbulence, systematic motions, outflows) in the direction of the centers of the cores, associated with star formation processes. In the G268.42–0.85 and G269.11–1.12 cores, the main factors causing line broadening can be both turbulence and systematic motions of the contraction type, the existence of which is indicated by a specific type of asymmetry in the profiles of optically thick lines (see Fig. 1).

6 Model estimates of parameters of radial density and velocity profiles in cores

An absorption dip is observed in the profiles of the optically thick $\text{HCO}^+(1-0)$ and $\text{HCN}(1-0)$ lines in the G268.42–0.85 and G269.11–1.12 cores (Fig. 1). Its position is close to the peak position of $\text{H}^{13}\text{CO}^+(1-0)$ and other lines with a small optical depth. The red and blue wings of the lines, separated by the dip, have different amplitudes, with the blue peak exceeding the red one over significant part of the observed maps. The presence of asymmetry of this type for optically thick lines and symmetrical, close to Gaussian, profiles of optically thin lines, the maximum of which is close to the position of the dip in optically thick lines, indicates a probable contraction of the core [58]. Comparison of such spectral maps with maps calculated within non-LTE models can provide information about the distribution

of physical parameters, including the contraction velocity. This information can be used to select one or another theoretical model. The difficulty of finding optimal values when varying several parameters simultaneously is due to the fact that the error function may have more than one local minimum, and the parameters themselves may correlate with each other, which leads to dependence on initial conditions and poor convergence. To overcome these difficulties, an algorithm was proposed in [12] based on the use of statistical methods of principal components (PC) and k-nearest neighbors (kNN) for fitting model spectral maps into observed ones.

The $\text{HCO}^+(1-0)$ spectra with a dip and asymmetry were observed in the central part of the G268.42–0.85 core and in the northern part of the G269.11–1.12 core. To estimate radial profiles of physical parameters, a multilayer spherically symmetric model is used, the parameters of which (density, turbulent, systematic velocity and kinetic temperature) depend on the radial distance according to the law: $P = P_0/(1 + (r/R_0)^{\alpha_p})$, where R_0 is the radius of the central layer, taken equal to 2×10^{16} cm. The description of the model is given in [12]. The morphology of molecular emission regions, as well as the structure of inner regions of the cores according to the 350 μm data, shows differences from spherical symmetry (see Figs. 2, 3). The use of a spherically symmetric model in this case can provide information about the averaged radial profiles of physical parameters in the outer regions of the cores.

The model parameters are the values of P_0 for density, turbulent and systematic velocity radial profiles (n_0, V_{turb}, V_{sys} , respectively), the corresponding power-law indices α_p ($\alpha_n, \alpha_{turb}, \alpha_{sys}$), as well as the relative abundances of HCO^+ and H^{13}CO^+ , considered to be independent of the radial distance, the outer radius of the model cloud (R_{max}) and the source Doppler velocity (V_{LSR}). Note, that in accordance with the given type of radial profiles, the values of physical parameters in the central layer are equal to half of the corresponding n_0 ,

V_{turb} and V_{sys} values. The kinetic temperature profile has the form $T = 80 \text{ K}/(1 + (r/R_0)^{0.3})$ and is not changed during the calculations. We used the values of the $\text{HCO}^+ - \text{H}_2$ collision probabilities from [59], calculated for fixed temperatures with increments of 10 K. Accordingly, the temperature in each layer is rounded to a multiple of 10 K. Thus, the kinetic temperature in the model is equal to 40 K in central layers (which is close to the estimates of kinetic temperatures in G268.42 and G269.11, see Table 4) and dropped to $\sim 10 \text{ K}$ at the periphery. For the calculations, 14 layers are taken, the width of which increased according to a power law with increasing distance from the center. After calculating model spectra, convolution with the telescope radiation pattern is carried out and the error function is calculated, depending on the difference between the model and observed spectra at different points. To reduce information loss when calculating the error function, maps with a step of $6''$ in both coordinates are used, obtained as a result of processing the data with the *Gridzilla* package.

The methodology for applying the algorithm to find the global minimum of the error function corresponded to that given in [12] with some additions described in the Appendix. As part of the algorithm, a set of precedents is generated and probable model parameters and their confidence regions are estimated. The PC method is used to reduce the model dimension (from 10 to 6) and uniformly fill the parameter space. The kNN method is used to find optimal parameter values corresponding to the global minimum of the error function determined by the difference between the model and observed spectra (for more details, see [12]).

Model $\text{HCO}^+(1-0)$ and $\text{H}^{13}\text{CO}^+(1-0)$ line maps are fitted into the central region of G268.42–0.42 with a size of $\sim 1.5' \times 1.5'$, which corresponds to linear size $\sim 0.7 \text{ pc}$, as well as in the map of the northern part of G269.11–1.12 with a size of $\sim 1' \times 1.3'$ or $\sim 0.7 \times 1 \text{ pc}$. Since, within the framework of the model used, we are unable to achieve a satisfactory fit

of the model $\text{HCO}^+(1-0)$ maps into those observed in G269.11–1.12 (see Section 7), below we present the results of calculations only for the G268.42–0.42 core. Model and observed $\text{HCO}^+(1-0)$ and $\text{H}^{13}\text{CO}^+(1-0)$ line maps for this core are shown in Fig. 9. The values of the physical parameters for G268.42–0.42, corresponding to the minimum of the error function, as well as uncertainties of these estimates, corresponding to the boundaries of the confidence ranges obtained from the analysis of projections of the multidimensional error function on the plane of various pairs of parameters (Fig. 10), are given in Table 7.

Table 7: Model values of physical parameters of the G268.42–0.85 core

Parameter	Initial range	Value
$n_0(\text{cm}^{-3}), 10^7$	$0.6 \div 10$	$5.5^{+8.0}_{-4.3}$
α_n	$1.3 \div 2.0$	$1.6^{+0.2}_{-0.2}$
$V_{turb} \text{ (km/s)}$	$3 \div 9$	$6.7^{+1.4}_{-2.3}$
α_{turb}	$-0.2 \div 2.1$	$0.2^{+0.1}_{-0.1}$
$V_{sys} \text{ (km/s)}$	$-1.5 \div -0.1$	$-1.2^{+0.2}_{-0.5}$
α_{sys}	$-0.6 \div 0.6$	$-0.5^{+0.3}_{-0.2}$
$R_{max} \text{ (pc)}$	$0.2 \div 4$	$4.6^{+2.1}_{-3.2}$
$X(\text{HCO}^+), 10^{-10}$	$0.2 \div 20$	$1.5^{+3.3}_{-0.5}$
$X(\text{H}^{13}\text{CO}^+), 10^{-11}$	$0.2 \div 10$	$1.0^{+0.3}_{-0.2}$

n_0 , V_{turb} and V_{sys} represent double values of the parameters in the central layer

7 Discussion

The studied regions contain dense cores, associated with the regions of formation of massive stars and stars in clusters, as indicated by the presence of high-luminosity IRAS sources, compact H II regions, methanol and water masers, near-infrared sources, and other sources

(see Section 2). From observations, it follows that the studied regions have rich molecular composition (see Table 5), which is typical for the cores associated with regions of formation of high-mass stars or stars in clusters. Core 1 from the G285.26–0.05 region is poorer in chemical composition than the others.

The calculated kinetic temperatures (see Table 4) demonstrate both closeness and discrepancies with independent estimates. Thus, for G268.42, the calculated kinetic temperature is close to the estimate from [51] (33 K), obtained from observations of methyl cyanide lines in the $J = 6 - 5$ transition, as well as to the dust temperature (35 K [18]). The kinetic temperature estimate in G270.26 from methyl acetylene, taking into account the error, practically coincides with the dust temperature estimate (29 K [18]), but is slightly lower than the peak CO(1–0) line temperature (44 K [13]), which in the case of large optical depth can serve as a measure of kinetic temperature. The kinetic temperature estimate in G294.97, taking into account the error, exceeds the estimate of the dust temperature in the direction of the IRAS source (27 K [18]) and is close to the value of the peak temperature of CO(1–0) (41 K [13]). The difference in kinetic temperatures in G291.27, calculated using methyl acetylene and methyl cyanide lines, is beyond the error limits (see Table 4). Observations in ammonia lines with an angular resolution of $\sim 11''$ [60] showed that the kinetic temperature in the core can vary from ~ 30 K to ~ 50 K in the region where we calculated the average kinetic temperatures. It is possible that the spatial distributions of emission in the methyl acetylene and methyl cyanide lines on scales smaller than the size of the MOPRA-22m beam in a given region differ from each other, which leads to differences in temperature estimates. New observations in these lines with better angular resolution (for example, $\sim 10''$) could be useful in answering the question of the reason for the discrepancy in the estimates obtained.

Virial masses calculated from different lines (Table 6) differ from each other, often exceeding the error limits ($\sim 10 - 50\%$), which may be due to differences in the sizes of emission

regions, line widths, excitation conditions for various species, as well as variations in the chemical composition in the cores. For the cores of G268.42, G269.11, and G291.27, the masses calculated from dust emission data [20] lie in the range of virial estimates. For the remaining cores (especially for G294.97), the virial masses exceed the masses calculated from dust. It should be noted that the estimates of M_{VIR} may be overestimated. An increase in line widths in the inner regions of the G268.42, G269.11 and G270.26 cores ($b \lesssim 0.3 - 0.6$ pc) (Fig. 8) is apparently associated with the influence of internal sources, which cause an increase in the dispersion of non-thermal velocities and increase the average values of ΔV and M_{VIR} . If the cores are inhomogeneous, then virial masses will be lower. Thus, for the density profile r^{-2} , the virial masses will be 40% less than the values given in Table 6.

The cores differ in their internal kinematics, as indicated by different profiles of the optically thick lines $\text{HCO}^+(1-0)$ and $\text{HCN}(1-0)$ (Fig. 1), as well as the different shapes of the radial profiles of non-thermal velocity dispersion (Fig. 8). In two cores (G268.42–0.85, G269.11–1.12), an asymmetry of the $\text{HCO}^+(1-0)$ profiles indicates probable gas contraction. Using a detailed analysis of the $\text{HCO}^+(1-0)$ and $\text{H}^{13}\text{CO}^+(1-0)$ line maps with a spherically symmetric model, the parameters of the radial dependences of density, turbulent velocity dispersion, and contraction velocity in the G268.42–0.85 core are estimated (Table 7). The results of model calculations of $\text{HCO}^+(1-0)$ and $\text{H}^{13}\text{CO}^+(1-0)$ generally describe the observed spectra in G268.42–85 quite well, although there are some discrepancies between model and observed $\text{HCO}^+(1-0)$ line profiles in the northeastern part of the core (see Fig. 9). For G269.11–1.12, the model and observed spectra are consistent only in the center of the core, while in the northeastern and southwestern parts the discrepancies in both the peak temperature values and the form of line profiles turned out to be very significant. These discrepancies may be associated with the difference in the shape of the cores from spherical symmetry, as well as with an influence of rotation, which can lead to differences in the form

of the $\text{HCO}^+(1-0)$ line profiles from those expected in the case of radial contraction. The G269.11-1.12 core is more elongated (compare the ratios of the axes of the fitted ellipses for G268.42 and G269.11, Table 6). In addition, model estimates of physical parameters in G269.11-1.12 differ from independent estimates. It is possible that the model used is too simplified to describe this core.

For the G268.42–0.85 core, the calculated model parameters (see Table 7) are consistent with independent estimates, taking into account uncertainties of the compared quantities. Note, that the obtained outer radius value (~ 4 pc) represents the boundary of the model cloud and cannot be directly compared with the observed sizes of emission regions in molecular lines (see Table 6). In addition, an uncertainty of this value, calculated from the confidence range, reaches $\sim 70\%$ (see Table 7). Due to a sharp decrease in density, the outer layers of the model cloud with low density ($< 10^4 \text{ cm}^{-3}$ for $r > 1$ pc) affect primarily the magnitude of the dip in the profiles of optically thick lines, absorbing radiation from the central layers, and practically do not contribute when estimating the sizes of emission regions at half the maximum level. Taking into account large uncertainty in the density value in the central layer ($\sim 100\%$, Table 7), the model column densities of molecular hydrogen averaged for the region of $\sim 24''$ (~ 0.2 pc) and the masses for the HCO^+ and H^{13}CO^+ emission regions (~ 0.6 pc, Table 7) are easy to reconcile with the corresponding values $N(\text{H}_2)$ and M_{VIR} from Tables 5, 6. A power-law index of the radial density profile obtained from the model coincides with the value obtained from the 1.2 mm observations [21]. The estimate of the power-law index of the radial density profile for G269.11-1.12, obtained from model calculations, is significantly lower than the index calculated from observations of dust emission (1.2 and 2 [21], respectively).

The ratio of model abundances $[\text{HCO}^+]/[\text{H}^{13}\text{CO}^+]$ in G268.42–0.85 is lower than the range of probable values of the $^{12}\text{C}/^{13}\text{C}$ ratio ($\sim 35 - 55$), calculated from the dependence from

[61] for a galactocentric distance $R_G \sim 8.7$ kpc. The uncertainty in the model abundance ratio is, however, rather high (Table 7). The model estimate of $X(\text{H}^{13}\text{CO}^+)$ for G268.42–0.85 coincides with the estimate obtained from LTE calculations (Table 6). For G269.11–1.12 these estimates differ.

Turbulent velocity decreases with radial distance from ~ 3.3 km/s in the central layer to 1.5 km/s in the outer layer. Similar dependence was obtained previously for the L1287 core [12]. The contraction velocity in the central layer of G268.42–0.85 is ~ -0.6 km/s, which is close to the estimate of the two-layer model [62], obtained from the parameters of the observed $\text{HCO}^+(1-0)$ line profile for the point $(0'', -15'')$. The model power-law index of the radial profile of the contraction velocity, taking into account uncertainties, turned out to be less than zero ($\alpha_{sys} \sim -0.5^{+0.3}_{-0.2}$), which for a given type of model dependence means an increase in the contraction velocity in absolute value with increasing distance from the center.

This result differs both from the case of gas collapse onto a protostar in the free fall mode ($\alpha_{sys} = 0.5$) [3, 5, 7], and from the case of a non-equilibrium core in the mode of global hierarchical collapse with a constant velocity ($\alpha_{sys} = 0$) [10, 7]. However, the fact that for a part of the $\text{HCO}^+(1-0)$ map in G268.42–0.85 we are unable to reproduce completely the form of the line profiles (Fig. 9) indicates the likelihood of the existence of a more complex spatial distribution of systematic velocities in the core compared to the radial contraction. Taking into account the core rotation, indications of which were reported in [17], could possibly be useful for model calculations in this case. Contribution of rotation to the overall systematic velocity along the line of sight will obviously be different for different parts of the core, which should change the ratio of the intensities of the “blue” and “red” peaks of the profiles and, possibly, more accurately reproduce the features of the observed spectra in different parts of the map and correct the parameters of the radial contraction velocity profile.

Thus, an analysis of the results of model calculations showed that the used spherically symmetric model with single power-law indices of the physical parameter radial profiles is simplified for the cores under consideration. Nevertheless, with the help of this model, using the developed algorithm for fitting model spectral maps into observed ones [12], we are able to reproduce the $\text{HCO}^+(1-0)$ and $\text{H}^{13}\text{CO}^+(1-0)$ line maps observed in the G268.42–0.85 core and to estimate radial profiles of physical parameters. As in the L1287 core [12], the calculated value of α_{sys} differs from that expected in the case of free fall of gas onto a protostar [3, 5]. In this case, however, the found value does not agree with the prediction of the global collapse model [10, 7]. To verify the obtained result, it is necessary to carry out observations of this core with better sensitivity and higher spectral resolution both in 1–0 and in higher transitions of the rotational spectrum of HCO^+ and H^{13}CO^+ molecules, as well as to use for analysis the models that take into account both radial motions and gas rotation, as well as the difference from spherical symmetry. To obtain statistically significant conclusions about the nature of gas contraction in the cores associated with the regions of high-mass stars and star clusters formation, it is important to further expand the number of objects of analysis, where profiles of molecular lines, indicators of high density (HCO^+ , HCN , CS , etc.), have indications of contraction.

8 Conclusions

Using the 22-m radio telescope of the MOPRA observatory (Australia), spectral observations of six regions of formation of massive stars in the southern sky were carried out in the $\sim 84-92$ GHz frequency range in the lines $\text{CH}_3\text{OH}(5_{-1}-4_0 \text{ E})$, $c\text{-C}_3\text{H}_2(2_{1,2}-1_{0,1})$, $\text{CH}_3\text{C}_2\text{H}(5-4)$, $\text{H}^{13}\text{CN}(1-0)$, $\text{H}^{13}\text{CO}^+(1-0)$, $\text{SiO}(2-1)$, $\text{HN}^{13}\text{C}(1-0)$, $\text{HCN}(1-0)$, $\text{HCO}^+(1-0)$, $\text{HNC}(1-0)$, $\text{HC}_3\text{N}(10-9)$ and $\text{CH}_3\text{CN}(5-4)$. These regions have dense cores and are associated with bright IRAS point sources, compact H II regions, maser sources and near-infrared sources,

and have been observed previously in continuum and molecular lines. The following results are obtained:

1. The physical parameters of cores are determined, including kinetic temperatures ($\sim 30 - 50$ K), sizes of emission regions in various lines ($0.2 - 3.1$ pc) and virial masses ($\sim 70 - 4600 M_{\odot}$). The line widths significantly exceed the thermal widths ($\sim 2 - 5$ km/s). Within the framework of LTE, the column densities as well as the abundances of the H^{13}CN , H^{13}CO^+ , HN^{13}C , HC_3N , $c\text{-C}_3\text{H}_2$, SiO , $\text{CH}_3\text{C}_2\text{H}$ and CH_3CN molecules are calculated. The lowest abundances of H^{13}CN , H^{13}CO^+ and H_3CN are observed in the G285.26(1) core. The widths of various molecular lines, the optical depth of two of which is apparently small, increase in three cores with decreasing impact parameter, indicating the influence of the internal source on the dynamic activity of the gas. The difference between the line widths in the center and at the periphery in these objects reaches $\sim 1.5 - 2$ km/s.

2. An asymmetry of the optically thick $\text{HCO}^+(1-0)$ and $\text{HCN}(1-0)$ line profiles indicates the probable contraction of gas in the G268.42–0.85, G269.11–1.12 cores. Within the framework of a spherically symmetric model, using an algorithm for minimizing the error function when fitting model maps into observed ones [12], the optimal values of the parameters of density, turbulent velocity and contraction velocity radial profiles in the G268.42–0.85 core are calculated and their uncertainties are determined. Density decreases with distance from the center as $r^{-1.6}$, turbulent velocity decreases as $r^{-0.2}$, and contraction velocity increases as $r^{0.5}$. The radial profile of the contraction velocity differs from that expected both in the case of free fall of gas onto a protostar ($r^{-0.5}$), and in the case of global core collapse (contraction velocity does not depend on distance). A possible reason for this discrepancy could be rotation of the G268.42–0.85 core, which is not taken into account in the model.

Appendix

APPLICATION OF AN ALGORITHM FOR FINDING THE GLOBAL MINIMUM OF THE ERROR FUNCTION AND ESTIMATING CONFIDENCE INTERVALS OF MODEL PARAMETERS

In [12], to analyze the maps of molecular lines in the L1287 core, the excitation of molecules was simulated in a spherically symmetric model and model spectral maps corresponding to the observed ones were calculated. The optimal values of the model parameters and their confidence ranges were calculated using an original algorithm for finding the global minimum of the error function between the model and observed spectra at each point, including the PC method used for the statistical procedure of reducing the model dimension, and the kNN method for finding the optimal values.

This approach is applied to analyze the maps G268.42–0.85 and G269.11–1.12 in the HCO⁺(1–0), H¹³CO⁺(1–0) lines. Compared to the approach described in [12], the generation of model precedents before the application of the dimensionality reduction procedure is changed: when generating the sample, precedents are randomly excluded in accordance with the criterion:

$$\left(\sum_{k=1}^b r_k/\chi^2\right)/b < \alpha, \quad (1)$$

where

$$r_k = \sum_{i=1}^n \sqrt{(p_i^{new} - p_i)^2/\sigma_i^2} \quad (2)$$

is the normalized distance to previously generated model precedents of the parameter p_i (density, systematic and turbulent velocities). Normalization is carried out to the standard deviation σ_i of the parameter p_i for the previously generated data set. Here n is the number of parameters, p_i^{new} is the value of the parameter p_i to which criterion (1) is applied. When

calculating using formula (1), b precedents are used, selected according to the criterion of the minimum error function. The value p_i^{new} is randomly selected within the given ranges. The coefficients b and α are chosen empirically and are equal to 7 and 0.1, respectively. The precedents for which relation (1) is satisfied are discarded. For the rest, spectral maps are calculated, the error function is calculated, and the precedent is added to the total sample. Thus, we avoided calculating model parameters if a precedent with a larger value of the error function was previously calculated nearby.

The sample is produced in several generations (1000 implementations), some of which are discarded according to the criterion (1), except for the first generation. Next, the sample is randomly divided into two parts. For each, the transformation kernel of the nonlinear principal component method (with exponential nonlinearity) is calculated. If the conversion coefficients calculated for the full sample and for the parts did not differ by more than 10%, it is accepted that the dimensionality reduction procedure could be applied. Then, similarly to [12], precedents are calculated at the nodes of a regular grid for a space of reduced dimensionality. Generations are produced until doubling the number of precedents led to changes in estimates of the probable values of the parameters and their confidence ranges. Although these changes have little effect on filling the parameter space with precedents after applying dimensionality reduction procedures, they lead to an acceleration of the process of accumulating precedents before the reduction procedure. This fact is important, since with the accumulation of statistics, the percentage of discarded precedents is close to $\sim 95\%$ in the original version of the algorithm and $\sim 70\%$ in the modified version, which makes it possible to speed up preliminary calculations by ~ 6 times. This is achieved due to the fact that parameters for which k nearest implementations have a larger error function value can be discarded without carrying out model calculations. Although this modification is not critical when analyzing individual sources, it is necessary when analyzing multiple objects,

as it speeds up calculations without affecting the confidence of the final estimates.

Based on the modified algorithm, parameters of the G268.42–0.85 and G269.11–1.12 cores are estimated. A priori assumptions about initial ranges of parameter values and the obtained most probable values with the confidence ranges at the 1σ level for G268.42–0.85 are given in Table 7. The initial ranges of values, however, did not strictly define the boundaries of the areas filled by model precedents. When calculating the principal components, these areas could be automatically expanded (as in the case of R_{max}). The corresponding spectral maps are shown in Fig. 9.

Figure 10 presents sets of two-dimensional projections of a 10-dimensional error function between the model and observed spectral maps of $\text{HCO}^+(1-0)$ in G268.42–0.85 on the plane of various pairs of parameters. This figure (at the top of each column) shows graphs of the projection of the error function on each of the parameters. In the diagrams, there is a global minimum of the error function. For each parameter the area where χ^2 is less than the confidence threshold is marked. Several parameters correlate with each other. A negative correlation is observed between R_{max} and X_{HCO^+} . Positive correlations are observed between α_n and n_0 , as well as between the turbulent velocity in the central layer and α_{turb} . Weaker correlations exist between n_0 and R_{max} (positive) and n_0 and X_{HCO^+} (negative). The most probable parameter values are estimated using the kNN method. They are marked by red crosses on two-dimensional projections and by red vertical lines on graphs of the χ^2 projections on individual parameters. Confidence regions are calculated using the χ^2_σ hyperplane cross-section of the error function. The projections of the sections of the error function by the χ^2_σ hyperplane are contours on the planes of pairs of parameters; they correspond to horizontal lines on the graphs (Fig. 10).

9 Acknowledgements

The authors express their gratitude to the reviewer for valuable comments and instructions, which significantly improved the text of the article. The work is supported by the Russian Science Foundation grant no. 23-22-00139.

References

- [1] J. C. Tan, M. Beltrán, P. Caselli, F. Fontani et al. A. Fuente, M. R. Krumholz, C. F. McKee, and A. Stolte, Protostars and Planets VI, edited by H. Beuther, R. S. Klessen, C. P. Dullemond, and T. Henning (Tucson: University of Arizona Press, 2014) p. 149.
- [2] F. Motte, S. Bontemps, and F. Louvet, *Ann. Rev. A&A* 56, 41 (2018).
- [3] F. H. Shu *Astrophys. J.* 214, (1977).
- [4] F. H. Shu, F. C. Adams, S. Lizano *ARA&A* 25, 23 (1987).
- [5] C. F. McKee and J. C. Tan *Astrophys. J.* 585, 850 (2003).
- [6] Y. Zhang and J. C. Tan *Astrophys. J.* 853:18 (24pp) (2018).
- [7] E. Vázquez-Semadeni, A. Palau, J. Ballesteros-Paredes, G. C. Gómez, and Manuel Zamora-Avilés *MNRAS* 490, 3061 (2019).
- [8] R. B. Larson *MNRAS* 145, 271 (1969).
- [9] M. V. Penston *MNRAS* 144, 425 (1969).
- [10] Naranjo-Romero R., Vazquez-Semadeni E., Loughnane R.M. *ApJ* 814:48 (11pp) (2015).
- [11] L. E. Pirogov, V. M. Shul'ga, I. I. Zinchenko, et al., *Astron. Rep.* 60, 904 (2016).
- [12] L. E. Pirogov and P. M. Zemlyanukha, *Astron. Rep.* 65, 82 (2021).

- [13] I. Zinchenko, K. Mattila, M. Toriseva *A&A Suppl.* 111, 95 (1995).
- [14] A. V. Lapinov, P. Schilke, M. Juvela, and I. I. Zinchenko *Astron. Astrophys.* 336, 1007-1023 (1998).
- [15] J. Harju, K. Lehtinen, R.S. Booth, and I. Zinchenko *A&A Suppl.* 132, 211 (1998).
- [16] I. Zinchenko, C. Henkel, R. Q. Mao *A&A* 361, 1079 (2000).
- [17] L. Pirogov, I. Zinchenko, P. Caselli, L. E. B. Johansson, P. C. Myers *A&A* 405, 639 (2003).
- [18] L. Pirogov, I. Zinchenko, P. Caselli, L. E. B. Johansson *A&A* 461, 523 (2007).
- [19] T. Liu, K.-T. Kim, H. Yoo et al. *ApJ* 829:59 (2016).
- [20] L. E. Pirogov, *Radiophys. Quantum Electron.* 64, 857 (2022).
- [21] L. E. Pirogov *Astron. Rep.* 53, 1127 (2009).
- [22] D. A. Ladeyschikov, O. S. Bayandina and A. M. Sobolev *AJ* 158:233 (2019)
- [23] K. V. Getman, E. D. Feigelson, M. A. Kuhn, P. S. Broos, and G. P. Garmire *AJ* 158:235 (2019).
- [24] A. Roman-Lopes, Z. Abraham, R. Ortiz and A. Rodriguez-Ardila *Mon. Not. R. Astron. Soc.* 394, 467 (2009).
- [25] B. A. Binder and M. S. Povich *ApJ* 864:136 (29pp) (2018).
- [26] D. Apai, H. Linz, Th. Henning, and B. Stecklum *A&A* 434, 987 (2005).
- [27] Ch. D. Tremblay, T. L. Bourke, J. A. Green, J. M. Dickey, O. Ivy Wong, and T. J. Galvin *Mon. Not. R. Astron. Soc.* 510, 593 (2022).

- [28] J. S. Urquhart, M. G. Hoare, S. L. Lumsden, R. D. Oudmaijer et al. *A&A* 507, 795 (2009)
- [29] T. Culverhouse, P. Ade, J. Bock, M. Bowden et al. (QUaD Collaboration) *ApJ Suppl.* 195:8 (2011).
- [30] S. L. Breen, S. P. Ellingsen *Mon. Not. R. Astron. Soc.* 416, 178 (2011).
- [31] J. L. Caswell *Publ. Astron. Soc. of Australia*, 2009, 26, 454-467.
- [32] M. A. Voronkov, J. L. Caswell, S. P. Ellingsen, J. A. Green, and S. L. Breen *Mon. Not. R. Astron. Soc.* 439, 2584 (2014)
- [33] S. L. Breen, Y. Contreras, J. R. Dawson, S. P. Ellingsen, M. A. Voronkov, T. P. McCarthy *Mon. Not. R. Astron. Soc.* 484, 5072 (2019).
- [34] Slysh, V. I. Kalenskii, S. V. Val'tts, I. E. Otrupcek, R. *Mon. Not. R. Astron. Soc.* 268, 464 (1994).
- [35] Val'tts, I. E. Ellingsen, S. P. Slysh, V. I. Kalenskii, S. V. Otrupcek, R. Larionov, G. M. *Mon. Not. R. Astron. Soc.* 317, 315 (2000).
- [36] Yang, WenjinXu, YeChen, XiEllingsen, Simon P.Lu, DengrongJu, BinggangLi, Yingjie *ApJS* 231, Issue 2, article id. 20, 12 pp. (2017).
- [37] R. Ortiz, A. Roman-Lopes, and Z. Abraham *A&A* 461, 949 (2007).
- [38] B. Neichel, M. R. Samal, H. Plana, A. Zavagno, A. Bernard, and T. Fusco *A&A* 576, A110 (2015). 7
- [39] C. M. Dutra, E. Bica, J. Soares, and B. Barbuy *A&A* 400, 533-539 (2003)
- [40] J. L. Caswell *Mon. Not. R. Astron. Soc.* 297, 215-235 (1998)

- [41] S. L. Breen, J. L. Caswell, S. P. Ellingsen and C. J. Phillips Mon. Not. R. Astron. Soc. 406, 1487 (2010).
- [42] Gaylard, M. J. MacLeod, G. C. Mon. Not. R. Astron. Soc. 262, 43 (1993).
- [43] P. J. Barnes, S. D. Ryder, S. N. O'Dougherty, L. E. Alvarez, A. S. Delgado-Navarro, A. M. Hopkins and J. C. Tan Mon. Not. R. Astron. Soc. 432, 2231 (2013).
- [44] C. Eswaraiah, S.-P. Lai, W.-P. Chen et al. ApJ 850:195 (2017).
- [45] Breen, S. L.; Ellingsen, S. P.; Caswell, J. L.; Green, J. A.; Voronkov, M. A.; Fuller, G. A.; Quinn, L. J.; Avison, A. Mon. Not. R. Astron. Soc. 426, 2189 (2012).
- [46] A. J. Walsh, M. G. Burton, A. R. Hyland and G. Robinson Mon. Not. R. Astron. Soc. 301, 640 (1998).
- [47] J. A. Green, J. L. Caswell, G. A. Fuller, A. Avison, S. L. Breen, S. P. Ellingsen, M. D. Gray, M. Pestalozzi, L. Quinn, M. A. Thompson and M. A. Voronkov Mon. Not. R. Astron. Soc. 420, 3108 (2012).
- [48] N. Ladd, C. Purcell, T. Wong, S. Robertson PASA 22, Issue 1, pp. 62-72 (2005).
- [49] S. Yu. Malafeev, I. I. Zinchenko, L. E. Pirogov, and L. E. B. Johansson, Astron. Lett. 31, 239 (2005).
- [50] A. V. Alakoz, S. V. Kalenskii, V. G. Promislov, L. E. B. Johansson, and A. Winnberg, Astron. Rep. 46, 551 (2002).
- [51] E. Araya, P. Hofner, S. Kurtz, L. Bronfman, S. DeDeo ApJS 157, 279 (2005).
- [52] J. G. Mangum, Y. L. Shirley Publ. Astron. Society Pacific 127, 266 (2015).
- [53] Sh.-P. Lai, T. Velusamy, W.D. Langer, and T.B.H. Kuiper Astron. J. 126, 311 (2003).

- [54] F. Bertoldi, C. F. McKee ApJ 395, 140 (1992)
- [55] V. Camacho, E. Vazquez-Semadeni, A. Palau, G. Busquet, M. Zamora-Aviles ApJ 903, id.46, 20 pp. (2020).
- [56] P. Caselli, P. J. Benson, P. C. Myers, M. Tafalla Astrophys. J. 572, 238 (2002).
- [57] T. G. Phillips, P. J. Huggins, P. G. Wannier, N. Z. Scoville Astrophys. J. 231, 720 (1979).
- [58] N. J. Evans II Ann. Rev. Astron. and Astrophys. 37, 311 (1999)
- [59] D. R. Flower MNRAS 305 651 (1999).
- [60] C. R. Purcell, V. Minier, S. N. Longmore, Ph. Andre, A. J. Walsh, P. Jones, F. Herpin, T. Hill, M. R. Cunningham, and M. G. Burton A&A 504, 139-159 (2009)
- [61] Y. T. Yan, J. S. Zhang, C. Henkel, T. Mufakharov, L. W. Jia, X. D. Tang, Y. J. Wu, J. Li, Z. A. Zeng, Y. X. Wang, Y. Q. Li, J. Huang, and J. M. Jian Astrophys. J. 877:154 (15pp), (2019).
- [62] Myers, P. C., Mardones, D., Tafalla, M., Williams, J. P., & Wilner, D. J. 1996, ApJ, 465, L133 (1996).

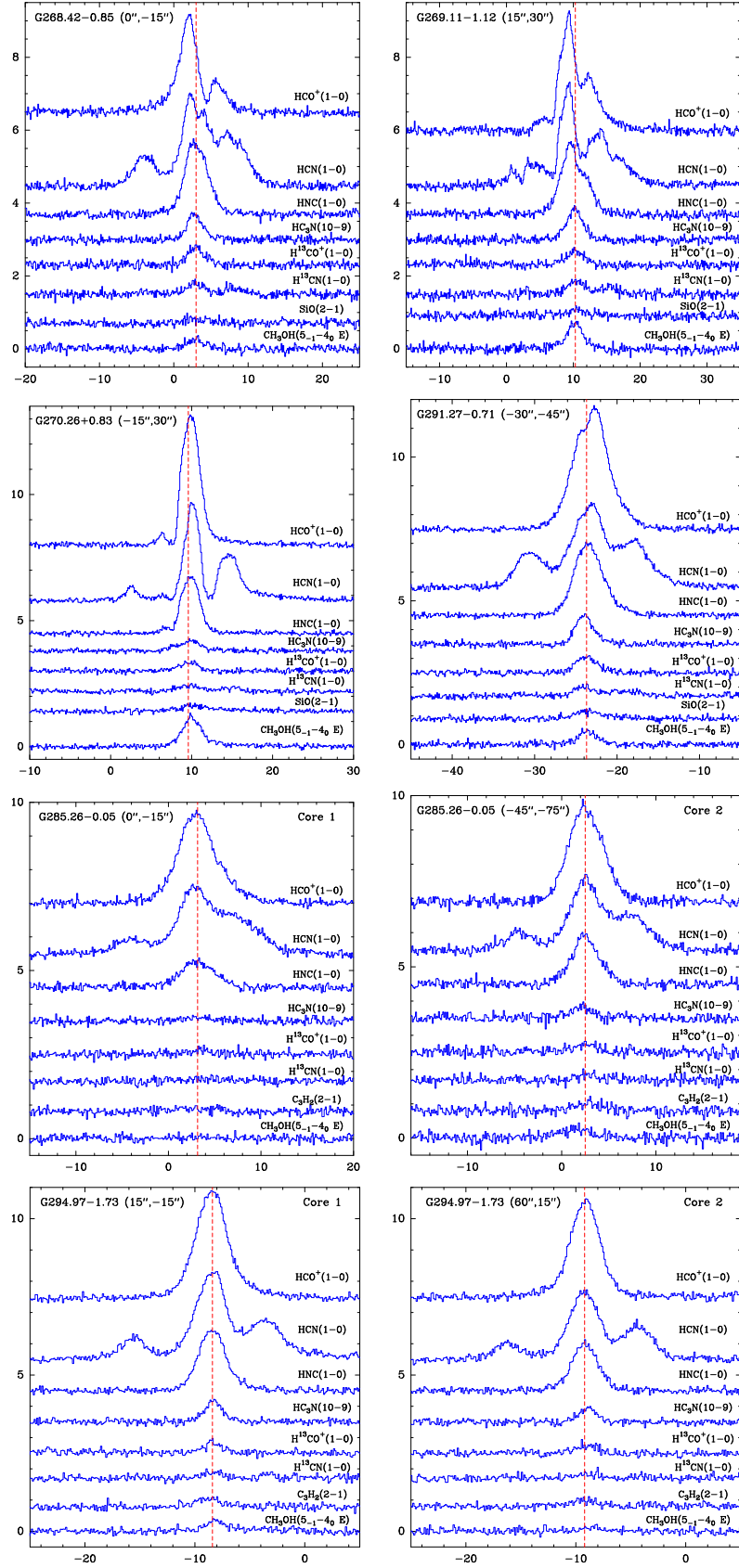


Figure 1: Spectra in the direction of emission peaks in objects. The horizontal axis shows the line of sight velocity, and the vertical axis shows the intensity in the telescope main beam temperature units (T_{MB}). For G285.26-0.05 and G294.97-1.73, the spectra are shown for two positions close to the centers of different cores in these objects. The dashed red lines correspond to the center of the optically thin $\text{H}^{13}\text{CO}^+(1-0)$ line.

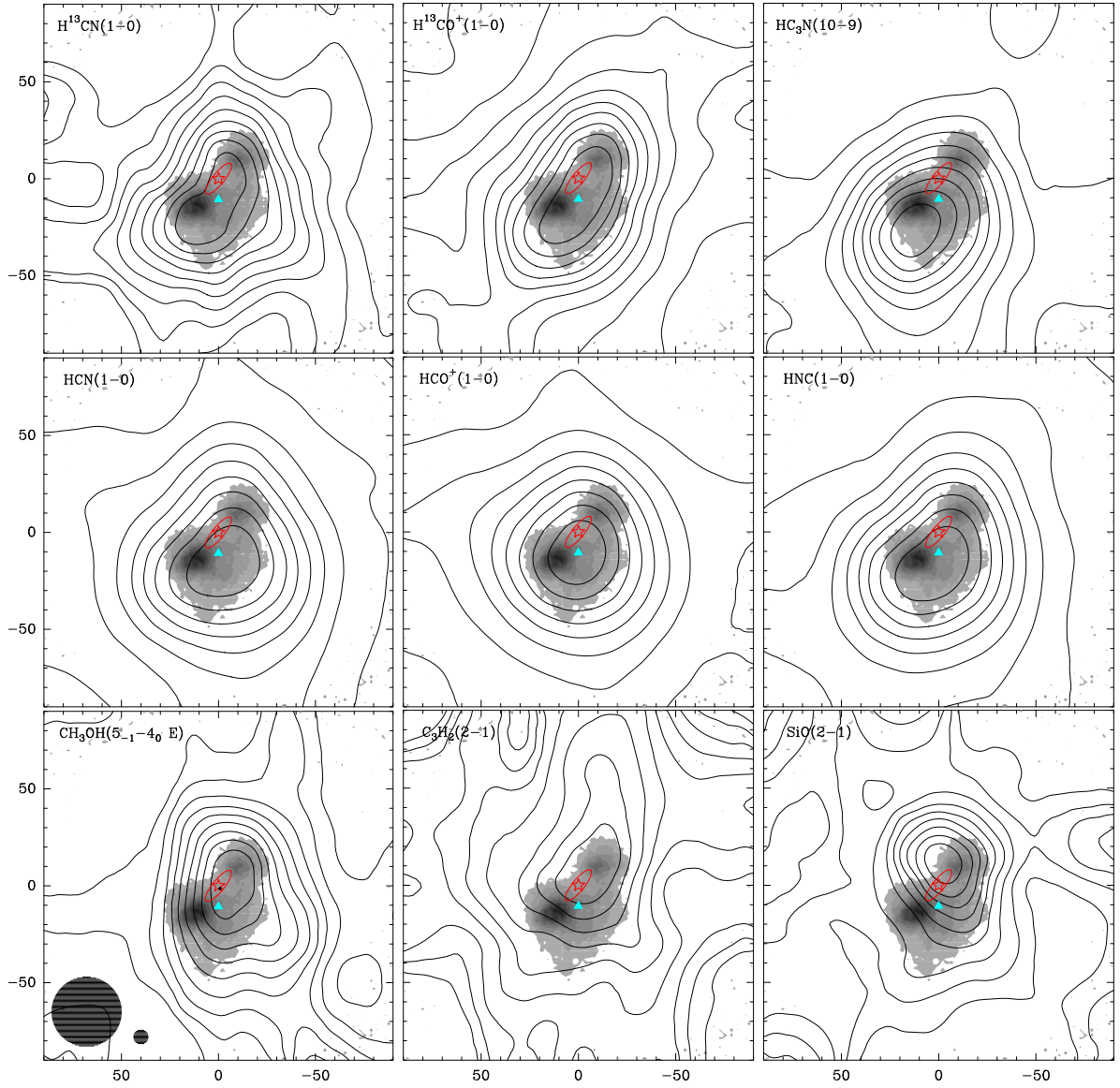


Figure 2: Maps of molecular lines observed in the G268.42–0.85 region (contours) and maps of dust emission in continuum at $350\ \mu\text{m}$ [20] (shades of gray). The axes show the offsets relative to the coordinates given in Table 1. Isolines of integrated intensities lie in the range from 10% to 90% of peak values (Table 1). The IRAS source is indicated by a red star, water maser [28] is indicated by a blue triangle. The uncertainty of the IRAS source position is shown by an ellipse corresponding to the 95% confidence level. The lower left corner of the CH_3OH map shows main beams of MOPRA-22m ($36''$) and APEX-12m ($7.5''$).

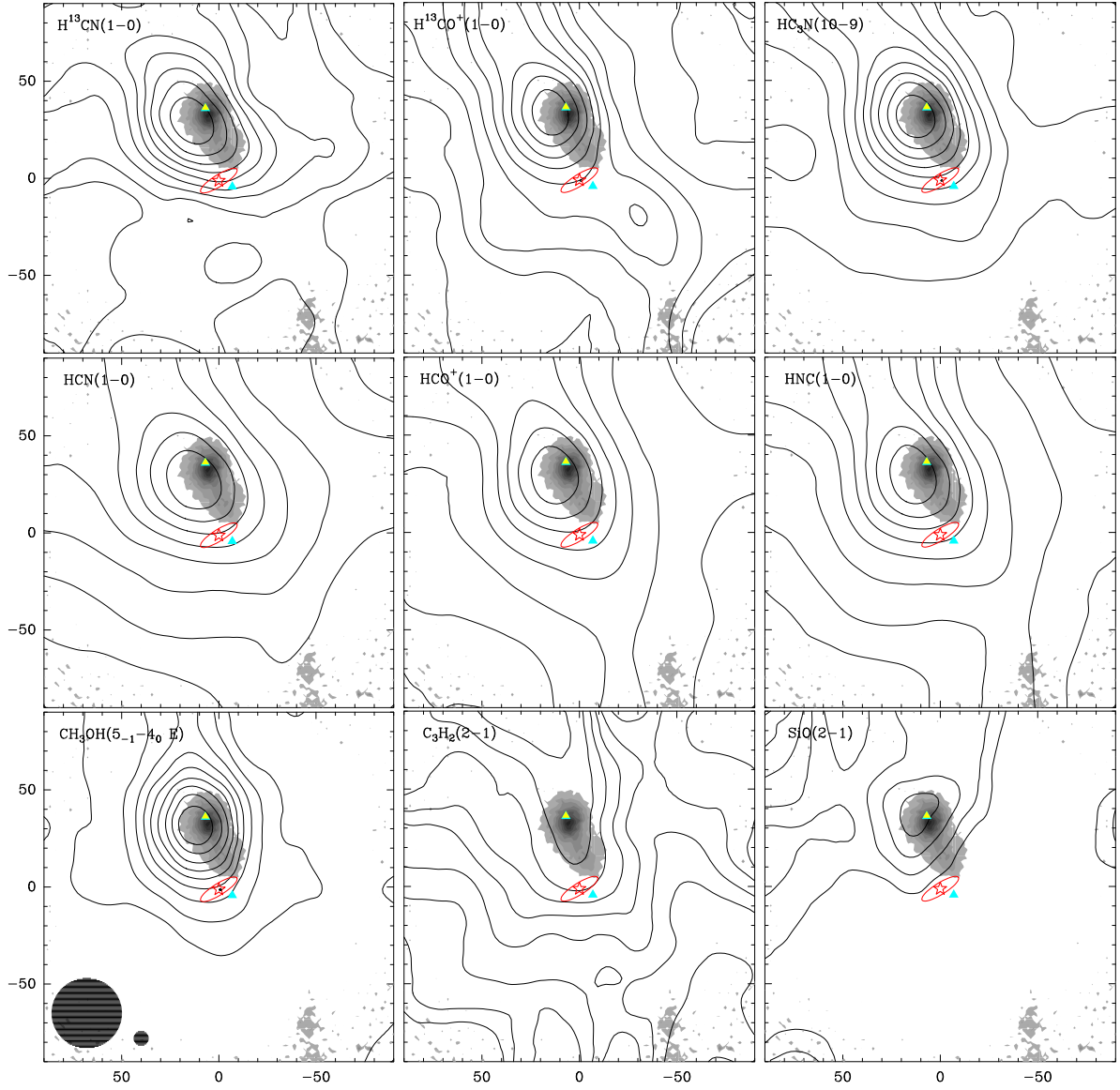


Figure 3: Maps of molecular lines observed in G269.11–1.12. A water maser is observed near the IRAS source [28]. Near the center of the core there is a water maser [30] and a class II methanol maser (6.7 GHz) [31]. Water and methanol masers are indicated by blue and yellow triangles, respectively. The remaining symbols are the same as in Fig. 2.

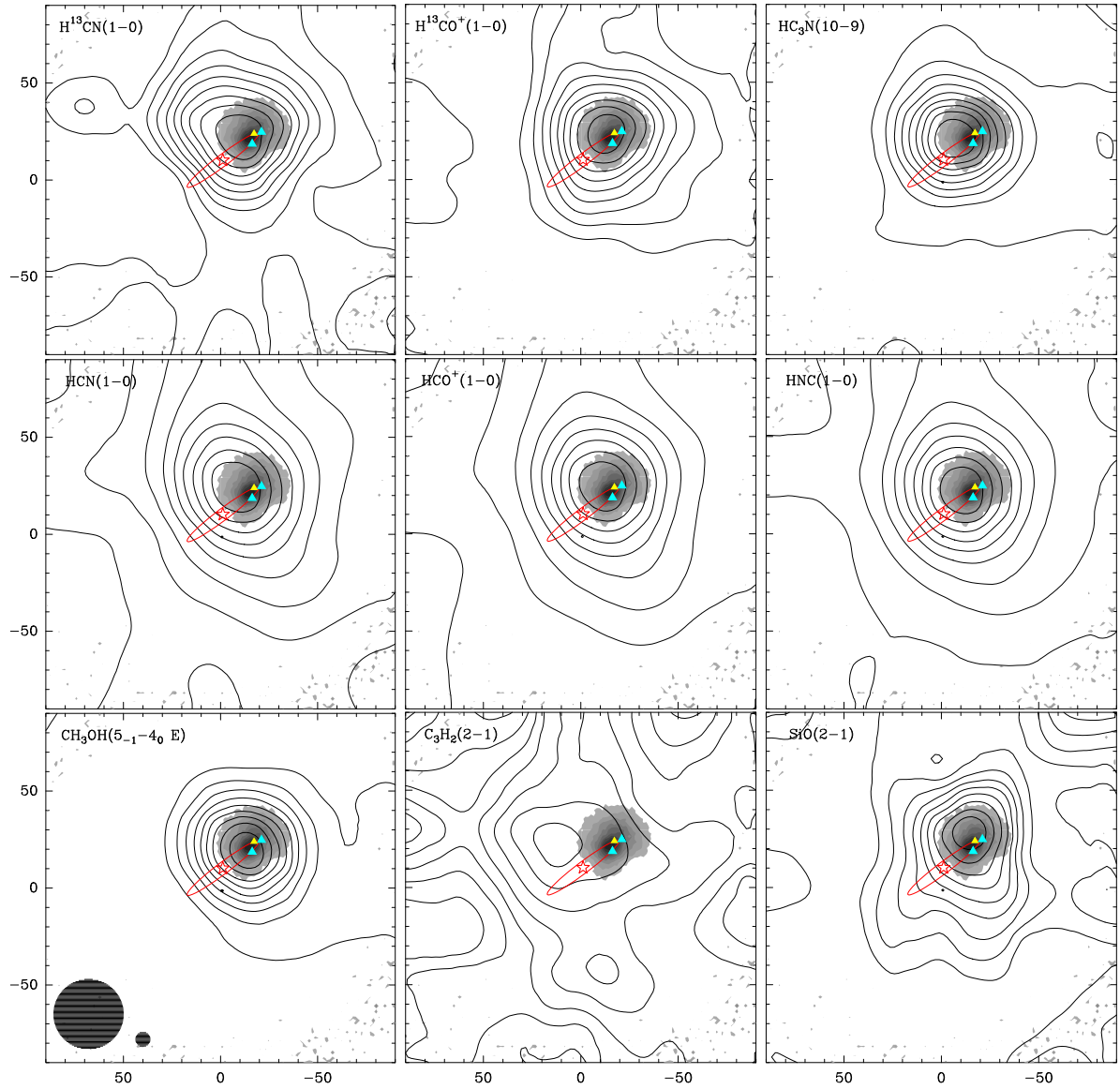


Figure 4: Maps of molecular lines observed in G270.26+0.83. Near the center of the core, water masers [30], indicated by blue triangles, and a class II methanol maser (6.7 GHz) [31], indicated by a yellow triangle, are observed. The remaining symbols are the same as in Fig. 2.

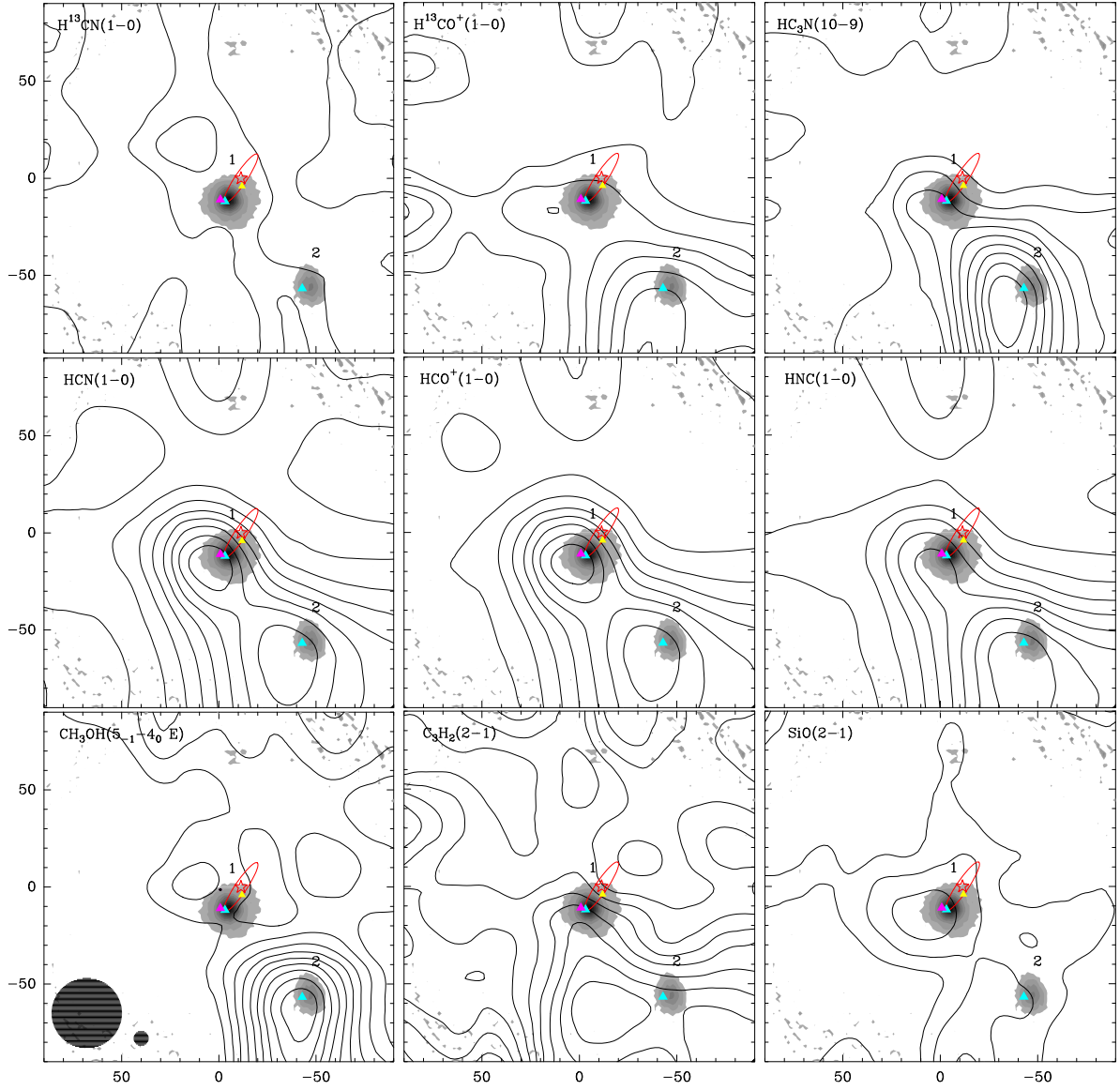


Figure 5: Maps of molecular lines observed in G285.26-0.05. Water masers [41] are indicated by blue triangles. A class II methanol maser (6.7 GHz) [42] and OH maser [40] are indicated by yellow and pink triangles, respectively. The remaining symbols are the same as in Fig. 2. The numbers indicate cores whose parameters are calculated separately.

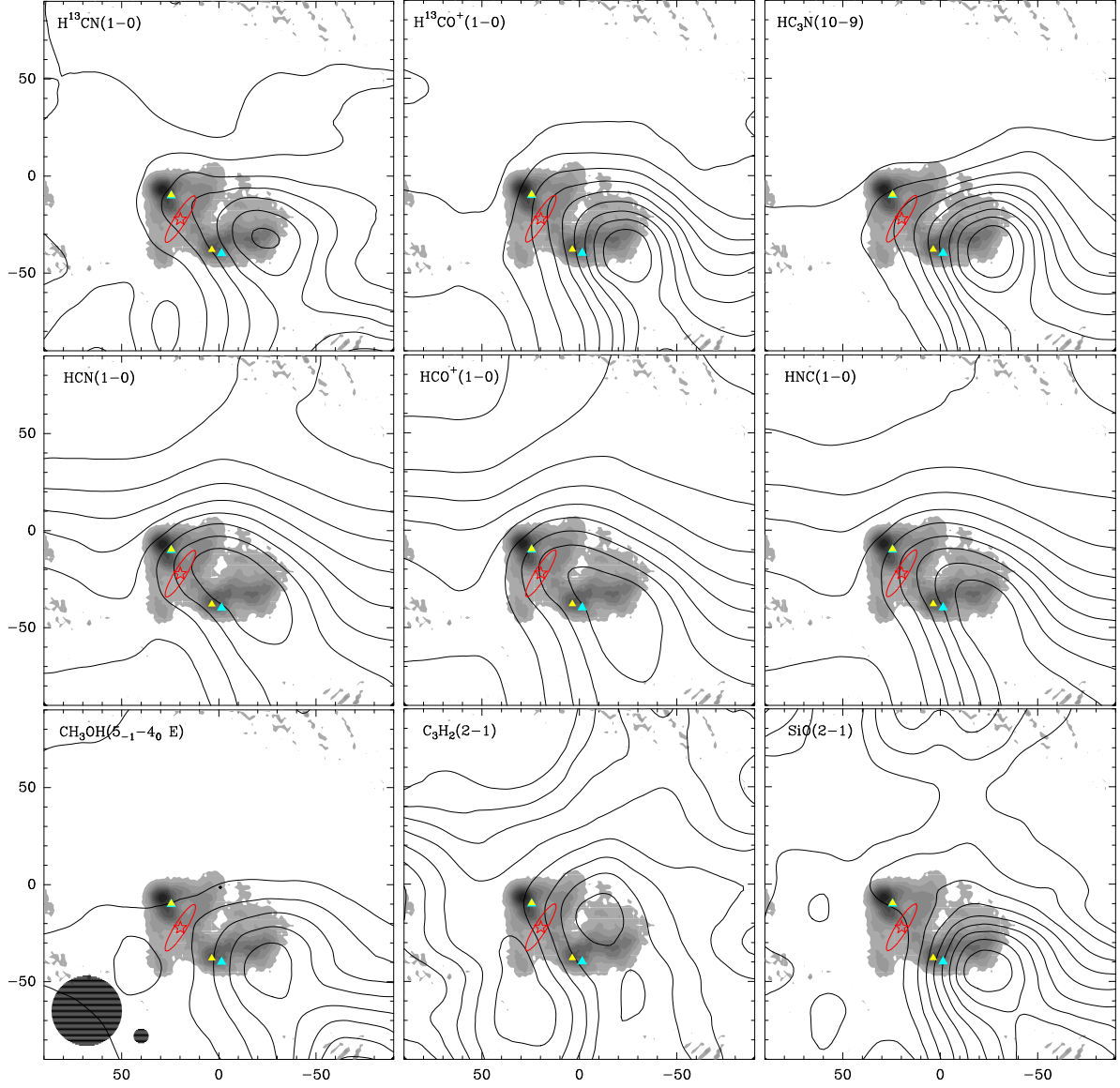


Figure 6: Maps of molecular lines observed in G291.27-0.71. Water masers [41] are indicated by blue triangles, class II methanol masers (6.7 GHz) [31] are indicated by yellow triangles. The remaining symbols are the same as in Fig. 2.

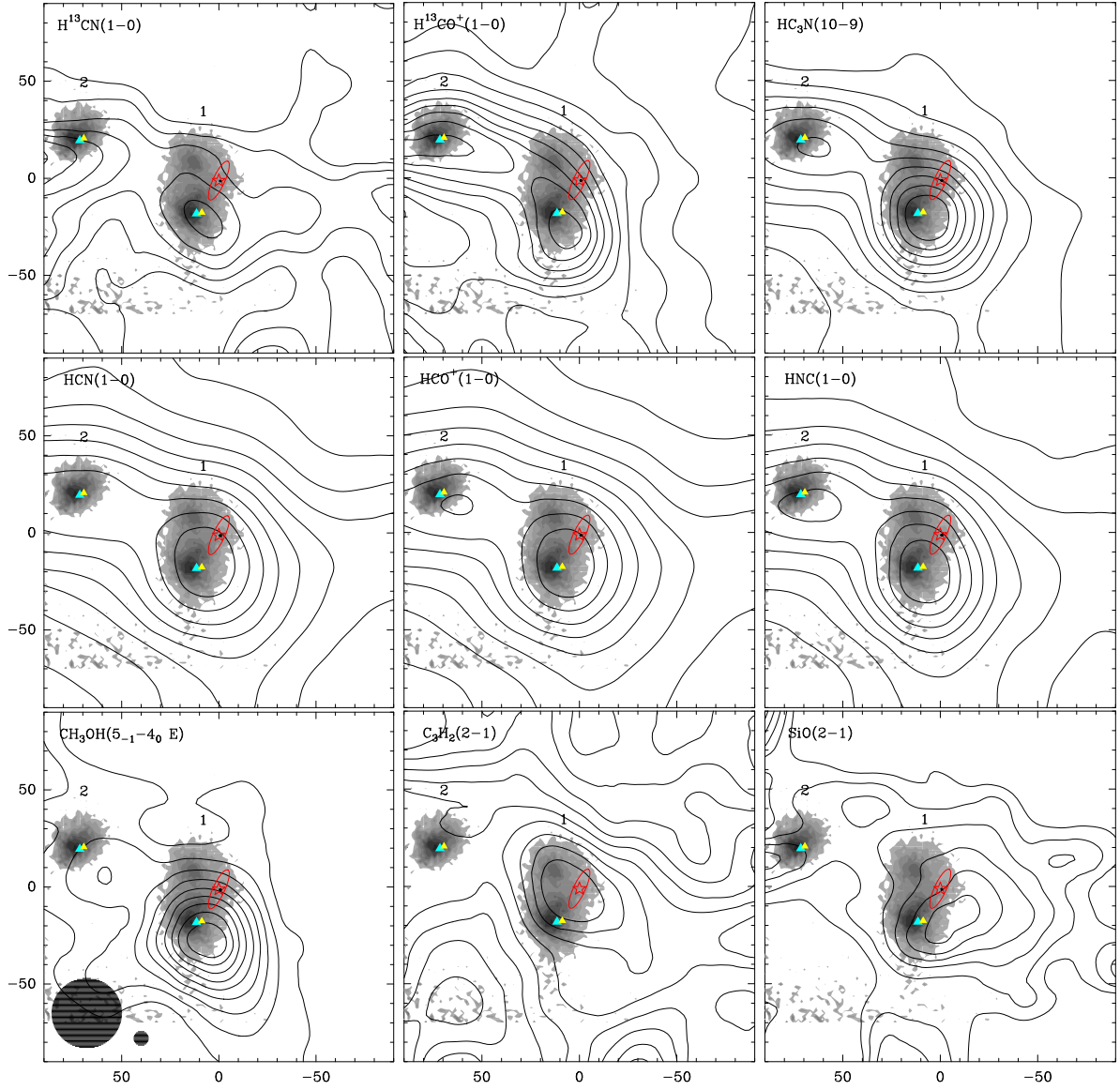


Figure 7: Maps of molecular lines observed in G294.97–1.73. Water masers [30] are indicated by blue triangles, class II methanol masers (6.7 GHz) [31, 47] are indicated by yellow triangles. The remaining symbols are the same as in Fig. 2. The numbers indicate cores whose parameters are calculated separately.

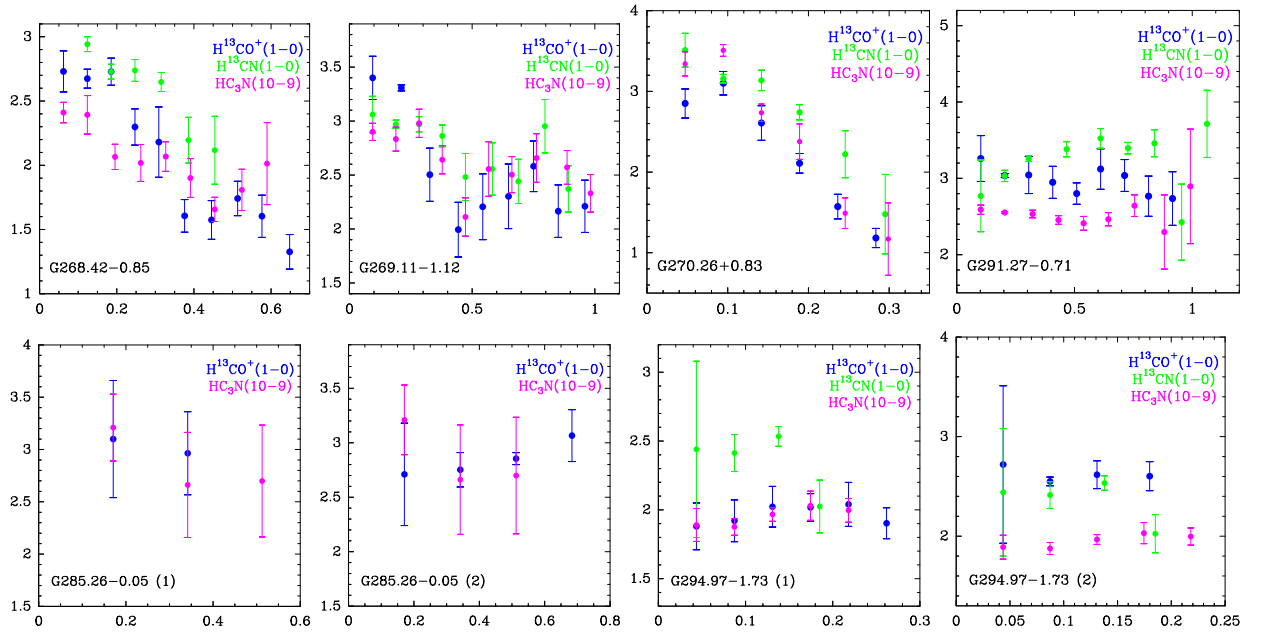


Figure 8: Profiles of the widths of optically thin lines of $\text{H}^{13}\text{CO}^+(1-0)$, $\text{H}^{13}\text{CN}(1-0)$ and $\text{HC}_3\text{N}(10-9)$, which are a measure of the dispersion of gas velocities in objects. The vertical axis shows the values of average widths in km/s (see text for details). The horizontal axis shows the impact parameters (b) in parsecs.

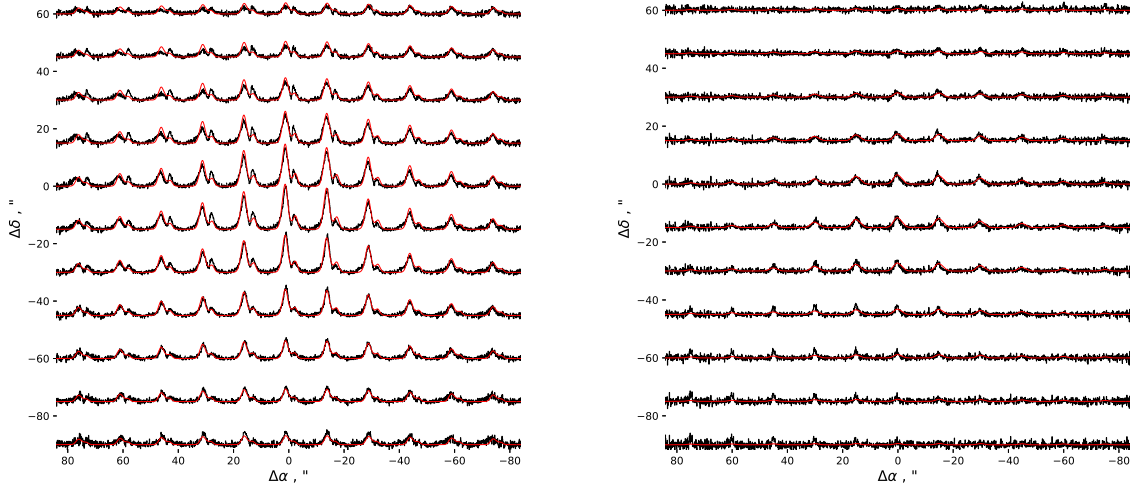


Figure 9: Maps in the $\text{HCO}^+(1-0)$ (left) and $\text{H}^{13}\text{CO}^+(1-0)$ (right) lines in the G268.42-0.85 core. The results of observations are shown in black. In red we show the results of model calculations corresponding to the obtained estimates of the physical parameters from Table 7.

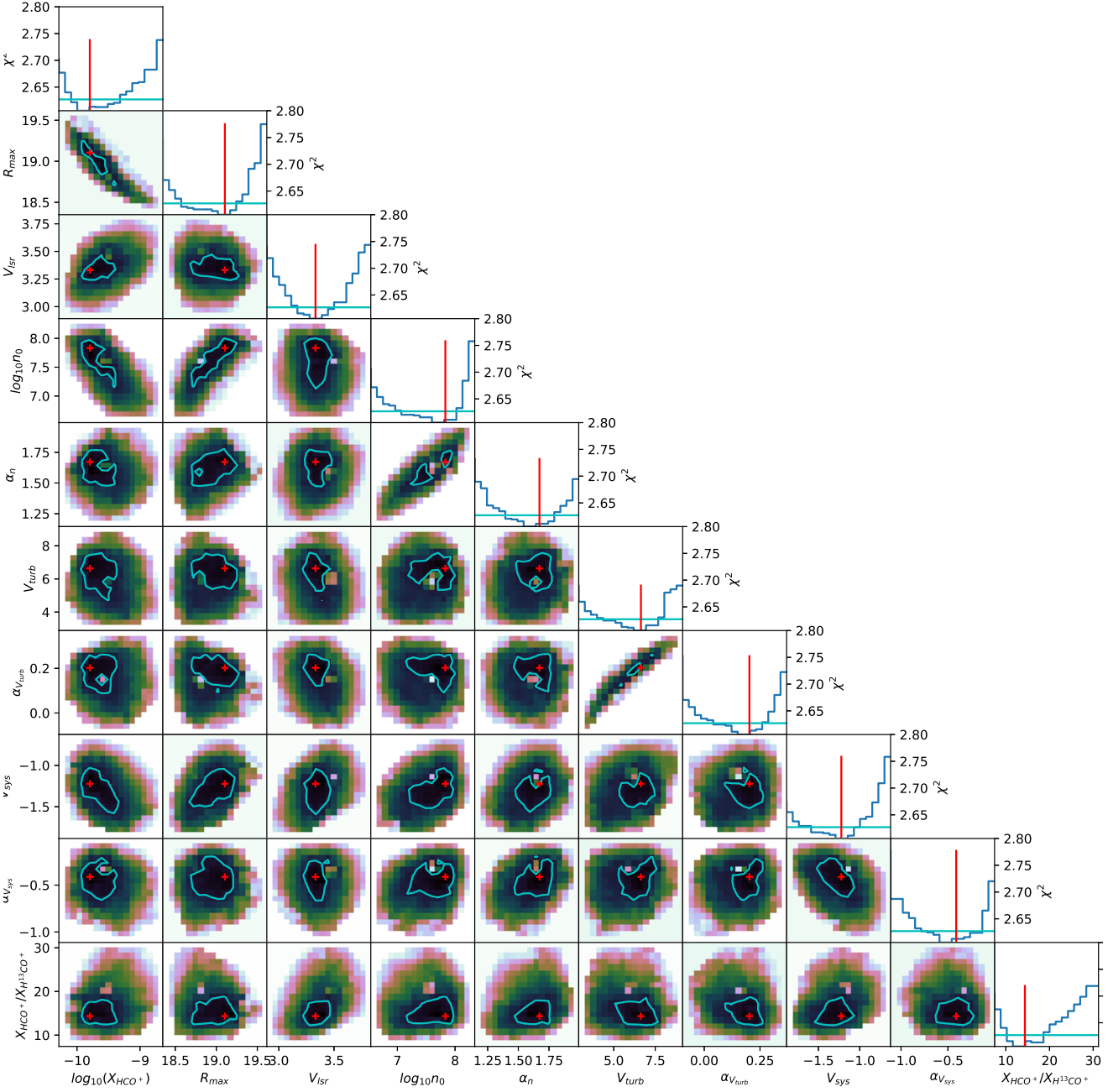


Figure 10: Projections of the 10-dimensional error function (χ^2) onto the plane of various pairs of parameters, calculated from fitting model spectral maps in the $\text{HCO}^+(1-0)$ and $\text{H}^{13}\text{CO}^+(1-0)$ lines into the observed maps in the G268.42–0.85 core. Above each column there are graphs of the error function depending on an individual parameter. The red dots in the diagrams and the red vertical lines in the top plots correspond to the global minimum of the error function obtained from the kNN method. Confidence regions for optimal parameter values, calculated from the χ^2_{σ} hyperplane section of the error function, are shown as blue contours and horizontal lines in the two-dimensional projections and one-dimensional plots, respectively.